Curing- and confinement-dependent mechanical behavior of loess-slag backfill: A fractal-informed constitutive interpretation

Lyu, Haoyan
School of Physics and New Energy, Xuzhou University of Technology

Wu, Peng
School of Physics and New Energy, Xuzhou University of Technology

Zhang, Lianying
School of Physics and New Energy, Xuzhou University of Technology

Shimada, Hideki
Department of Earth Resources Engineering, Faculty of Engineering, Kyushu University

他

出版情報：Results in Engineering. 29, pp.109753-, 2026-03. Elsevier
バージョン：

Results in Engineering 29 (2026) 109753

Contents lists available at ScienceDirect

Results in Engineering

journal homepage: www.sciencedirect.com/journal/results-in-engineering

Research paper

Curing- and confinement-dependent mechanical behavior of loess–slag backfill: A fractal-informed constitutive interpretation

Haoyan Lyu [a,b], Peng Wu [a,*], Lianying Zhang [a], Hideki Shimada [b], Takashi Sasaoka [b], Akihiro Hamanaka [b]

[a] School of Physics and New Energy, Xuzhou University of Technology, Xuzhou 221018, China
[b] Department of Earth Resources Engineering, Faculty of Engineering, Kyushu University, Fukuoka 819-0395, Japan

ARTICLE INFO

Keywords:
Loess–slag backfill
Mechanical behavior
Fractal dimension
Acoustic emission
Fractional-order constitutive model
Confinement effect
Triaxial compression

ABSTRACT

The mechanical performance of cemented backfill in deep engineering environments is jointly governed by curing-induced microstructural evolution and confinement-controlled deformation processes, yet their respective roles and interactions remain insufficiently understood. In this study, the curing- and confinement-dependent mechanical behavior of loess–slag backfill was investigated through triaxial compression tests, acoustic emission (AE) monitoring, mercury intrusion porosimetry (MIP), and a fractional-order constitutive interpretation focused on the stable hardening regime. Results indicate that curing primarily enhances intrinsic stiffness by refining pore network topology. This effect is quantitatively captured by the monotonic increase in the intact-state pore fractal dimension (D_{f0}) and its strong non-linear correlation with the generalized stiffness coefficient ($\mathbb{K}$). In contrast, confinement regulates the damage evolution pathway. The minimum AE b-value ($b_{\min}$) correlates strongly with the fractional order (α), revealing a fundamental transition from localized brittle cracking to distributed ductile deformation. Furthermore, post-peak softening behavior is shown to be closely linked to damage-induced fractal reorganization, with a strong monotonic relationship between the softening index B and the fractal-dimension increment ΔD_f, highlighting the role of fractal preservation in maintaining post-peak stability. Overall, this study provides a fractal-informed constitutive interpretation that clarifies how curing and confinement jointly control stiffness development, deformation mode, and failure stability of loess–slag backfill, offering insights for the design and optimization of cemented backfill systems under high-stress conditions.

List of symbols

σ	MPa Axial stress.
σ_3	MPa Confining pressure.
σ_{cd}	MPa Characteristic crack-damage stress.
ε	Axial strain.
ε_c	Characteristic strain at peak stress.
$\mathbb{K}$	GPa Generalized stiffness coefficient of the fractional constitutive relation.
α	Fractional order describing non-linear rheological behavior.
D_{f0}	Initial fractal dimension of the intact pore structure.
D_f	Fractal dimension of the post-failure pore structure.
ΔD_f	Fractal-dimension increment, defined as$D_{f0} - D_f$.
b	Acoustic emission b-value.
$b_{\min}$	Minimum b-value characterizing critical damage scaling.
RA	μs/V Rise angle of acoustic emission signals.
AF	kHz Average frequency of acoustic emission signals.
H	GPa Post-peak softening rate parameter.
B	Dimensionless brittleness index derived from post-peak response.
W_n	J Cumulative mercury intrusion work at intrusion step n.
Q_n	m^3 Cumulative mercury intrusion volume at intrusion step n.
r_n	M Pore radius corresponding to intrusion step n.

1. Introduction

Cemented backfill has become a critical component in modern underground engineering and mining operations, serving not only as a means of ground support but also as an effective strategy for waste

* Corresponding author.
E-mail addresses: lyu.haoyan.657@s.kyushu-u.ac.jp (H. Lyu), pengw@xzit.edu.cn (P. Wu).

https://doi.org/10.1016/j.rineng.2026.109753
Received 14 January 2026; Received in revised form 10 February 2026; Accepted 24 February 2026
Available online 25 February 2026

reutilization and sustainable construction [1–3]. In deep and ultra-deep environments, backfill materials are increasingly required to withstand high in-situ stresses while maintaining sufficient stiffness and ductility to ensure long-term stability [4–6]. Under such conditions, the mechanical performance of backfill is no longer governed solely by material composition, but by the coupled effects of curing-induced microstructural evolution and confinement-controlled deformation processes [7,8].

Loess–slag backfill, as a low-carbon cemented material incorporating industrial by-products, has attracted growing attention due to its economic and environmental advantages [9–11]. Previous studies have demonstrated that curing time plays a dominant role in strength development through hydration and geopolymerization reactions, leading to progressive densification of the pore structure and enhancement of load-bearing capacity [12–14]. Meanwhile, triaxial confinement has been shown to significantly alter failure modes, suppress tensile cracking, and promote ductile deformation in cemented backfill and similar geomaterials [15,16]. Despite these advances, curing and confinement are often treated as independent factors, and their distinct roles in controlling stiffness generation and failure stability remain insufficiently clarified.

From a microstructural perspective, conventional parameters such as porosity and average pore size are commonly used to describe the internal structure of cemented materials [17,18]. However, these Euclidean descriptors are often inadequate for capturing the inherent heterogeneity and connectivity of pore networks formed during hydration [19]. To address this limitation, fractal theory has been increasingly adopted to characterize the multi-scale complexity of pore structures in cementitious and geomaterials [20,21]. The fractal dimension provides a quantitative measure of space-filling capacity and topological complexity, offering deeper insight into how microstructural organization influences macroscopic mechanical behavior [22,23]. Nevertheless, most existing studies focus on static correlations between fractal descriptors and peak strength, while their role in constitutive stiffness and deformation evolution is rarely explored.

In parallel, acoustic emission (AE) monitoring has been widely employed to investigate damage evolution in rock and cemented materials under loading [24–26]. AE parameters, particularly the *b*-value, have been shown to reflect the scale distribution of microcracking events and the transition from distributed damage to localized failure [27,28]. While AE techniques provide valuable real-time insight into damage processes [29], their integration with microstructural descriptors remains largely qualitative. In many cases, AE observations are presented as supplementary evidence rather than being systematically linked to constitutive parameters or deformation mechanisms.

Constitutive modeling offers a powerful framework to bridge experimental observations and mechanical interpretation. Traditional elastic–plastic and damage-based models have been successfully applied to cemented backfill, yet they often rely on multiple empirical parameters and predefined damage criteria, limiting their physical transparency under varying stress paths [30–32]. In recent years, fractional-order constitutive formulations have attracted attention due to their ability to describe non-linear hardening behavior using a compact set of parameters [33–35]. Unlike conventional constitutive models where parameters are often treated as empirical regression coefficients with ambiguous physical meanings, the fractal-informed approach proposed in this study establishes a direct quantitative mapping between the mathematical fractional order (α) and the physical dynamic fractal dimension of damage ($b_{\min}$). This method advances current understanding by bridging the gap between micro-scale topological evolution and macro-scale rheological behavior, revealing that the non-linear hardening of backfill is fundamentally governed by the fractal organization of the damage network [36].

A further challenge lies in the characterization of post-peak behavior, which is crucial for assessing the stability and ductility of backfill systems. While peak strength is often emphasized, post-peak softening and residual load-bearing capacity are more directly related to deformation control and failure consequences in engineering practice [37,38]. Previous studies have shown that confinement can significantly mitigate post-peak softening, yet the microstructural origin of this effect remains debated [39,40]. In particular, the role of damage-induced structural reorganization in governing post-peak response has not been adequately quantified.

In this context, a unified interpretation that connects curing-driven microstructural evolution, confinement-controlled damage scaling, constitutive parameters, and post-peak behavior is still lacking. Specifically, three key questions remain unresolved: (i) how curing-induced pore topology evolution governs intrinsic stiffness development; (ii) how confinement regulates the scaling characteristics of damage evolution and deformation mode; and (iii) how post-peak softening can be interpreted in terms of structural complexity preservation or degradation.

To address these issues, this study investigates the mechanical behavior of loess–slag backfill through an integrated experimental–theoretical approach combining triaxial compression tests, MIP-based fractal characterization, AE scaling analysis, and fractional-order constitutive interpretation. By explicitly separating the stable hardening regime from post-peak failure, the intrinsic and extrinsic control mechanisms are decoupled and quantified. The proposed fractal-informed constitutive interpretation provides a physically grounded framework for understanding stiffness development, damage evolution, and post-peak stability of cemented backfill under high-stress conditions, offering insights for the rational design and optimization of sustainable backfill systems [41,42].

2. Materials and methods

2.1. Experimental materials

2.1.1. Cementitious materials

The selection of materials in this study is driven by the specific engineering and environmental context of mining districts in Western China. Loess, widely distributed in these regions, is typically treated as waste soil during surface stripping. Its utilization as a primary backfill aggregate eliminates the reliance on scarce river sand and significantly reduces transportation costs. Concurrently, Ground Granulated Blast-furnace Slag (GGBS), a major industrial by-product, is employed as a low-carbon binder substitute to mitigate the environmental footprint associated with Portland cement. The synergistic combination of locally sourced loess and slag not only addresses solid waste disposal challenges but also satisfies the mechanical requirements for deep underground backfilling, aligning with the industry's shift towards sustainable "Green Mining" practices.

The loess was obtained from a typical dump site associated with an open-pit coal mine and was air-dried and sieved to remove particles larger than 2 mm prior to use. The GGBFS, classified as S95 grade, served as the main reactive precursor in the binder system [11].

The chemical compositions of loess and slag were determined by X-ray fluorescence (XRF) analysis and are summarized in Table 1. The particle size distributions of both materials, measured by laser diffraction, are presented in Fig. 1. Compared with loess, the slag particles exhibit a generally finer size distribution, which is favorable for pore filling and matrix densification during curing.

Based on previous studies and preliminary investigations, a fixed slag-to-loess mass ratio of 7:3 was adopted for all specimens. This proportion has been shown to provide an optimal balance between workability and mechanical performance for loess–slag-based backfill materials, and was therefore kept constant throughout the experimental program to isolate the effects of curing time and confining pressure [9–11].

Table 1
Chemical composition of loess and slag.

Chemical composition (%)	SiO_2	Al_2O_3	CaO	Fe_2O_3	MgO	K_2O	Na_2O	TiO_2	MnO	SO_3
Loess	62.13	14.15	7.68	4.65	2.97	2.67	2.37	0.72	0.17	—
Slag	33.58	15.53	39.45	0.57	7.82	0.03	—	1.03	0.50	0.01

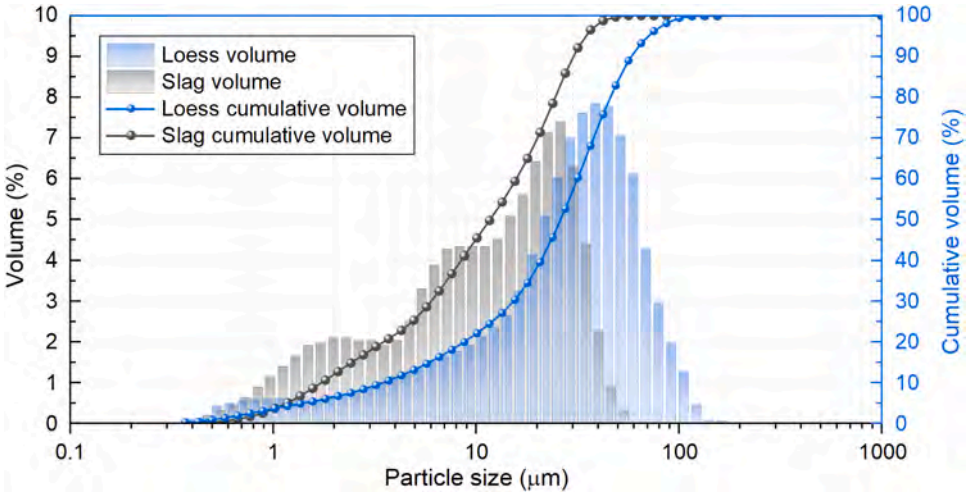

Fig. 1. Particle size distribution of loess and slag.

2.1.2. Alkaline activator

A composite alkaline activator was prepared using an industrial-grade sodium silicate solution and sodium hydroxide (NaOH) pellets. The initial sodium silicate solution had a modulus (molar ratio of SiO_2 to Na_2O) greater than 3.0. By dissolving a calculated amount of NaOH pellets into deionized water and subsequently mixing it with the sodium silicate solution, the modulus of the final activator was adjusted to 1.0.

This modulus was selected to balance solution workability and reactive ion availability, as values within the range of 0.8–1.2 are widely reported to be effective for activating slag-based geopolymer systems [43]. The activator solution was prepared in advance and allowed to cool to room temperature prior to mixing to ensure consistency across all batches.

2.1.3. Recycled aggregates

To align with sustainable mining and backfill practices, sulfur-free crushed sandstone was used as recycled aggregate, thereby avoiding potential adverse reactions associated with sulfide-containing materials. The Talbot power index was set to $n = 0.5$ to approximate the ideal Fuller gradation curve for maximum packing density. This particle size distribution minimizes the void ratio by ensuring that finer particles effectively fill the interstitial spaces between coarser aggregates, thereby enhancing the skeletal stiffness and compressive strength of the backfill matrix.

The maximum aggregate size was limited to 10 mm, satisfying the criterion of being less than one-fifth of the specimen diameter (50 mm). The aggregate was sieved into five size fractions (0–1.5, 1.5–3.0, 3.0–5.0, 5.0–8.0, and 8.0–10.0 mm), which were recombined according to mass proportions of 38.73 %, 16.04 %, 15.94 %, 18.73 %, and 10.56 %, respectively [44,45]. This gradation ensured good particle interlocking while maintaining sufficient slurry flowability during specimen preparation.

2.1.4. Mixing water

Deionized water was used for all mixing procedures and for preparing the alkaline activator solutions.

2.2. Specimen preparation

The preparation of loess–slag backfill specimens followed a standardized procedure comprising material weighing, mixing, molding, curing, and end-surface processing, as schematically illustrated in Fig. 2. The same preparation protocol was applied to all specimens to ensure consistency and comparability across different curing times and confining pressure conditions.

All constituent materials, including loess, slag, graded aggregates, alkaline activator, superplasticizer, and mixing water, were weighed according to the predetermined mix proportions. The alkaline activator solution was prepared in advance by dissolving NaOH pellets in deionized water, allowing the solution to cool to room temperature, and subsequently mixing it with the sodium silicate solution to achieve the target modulus. The dry components were first premixed to ensure uniformity, after which the activator solution and superplasticizer were added and mixed mechanically for 5 min until a homogeneous slurry was obtained.

The fresh slurry was poured into cylindrical PVC molds with an inner diameter of 50 mm and a height of 110 mm. To minimize air entrapment and segregation, the slurry was placed in two layers, with each layer subjected to mechanical vibration. After casting, the molds were sealed to prevent moisture loss. The specimens were demolded after 24 h and transferred to a standard curing chamber maintained at a temperature of 20 ± 1 °C and a relative humidity of $95 \pm 2\%$. Four curing times were considered: 1, 7, 14, and 28 days. Throughout the curing process, specimens were not immersed in water to avoid dissolution or leaching of the alkaline activator.

At the end of each curing time, the specimens were processed to meet the geometric and surface requirements for triaxial compression testing. Both ends of each specimen were cut and ground to achieve a final height of 100 mm, resulting in a height-to-diameter ratio of 2:1. The flatness and parallelism of the end surfaces were controlled within 0.02 mm and 0.05 mm, respectively, to minimize boundary effects during loading.

To support subsequent microstructural and post-failure analyses, two categories of specimens were prepared following curing. One group of specimens was reserved in the intact state for initial pore structure

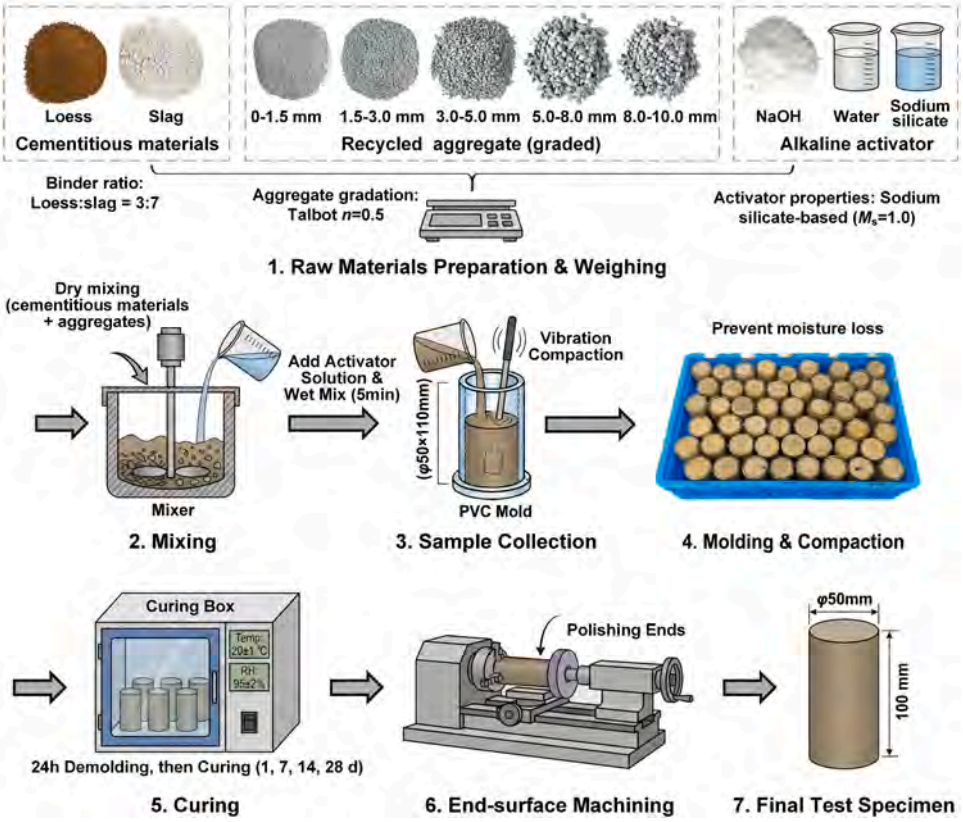

Fig. 2. Schematic of specimen preparation process.

characterization using mercury intrusion porosimetry (MIP). The remaining specimens were subjected to triaxial compression testing until failure, after which representative fragments were carefully collected from the interior and near the primary fracture zones for post-failure microstructural and pore structure analyses. This preparation strategy ensured consistency between mechanical testing and microstructural characterization.

2.3. Test methods and procedures

2.3.1. Triaxial compression test

Triaxial compression tests were conducted using a TATW-2000 servo-hydraulic rock mechanics testing system, as illustrated in Fig. 3. All triaxial compression tests were performed in strict accordance with the ASTM D7012–14 standard. Four confining pressure levels were considered: 0 MPa (uniaxial compression), 2 MPa, 4 MPa, and 6 MPa.

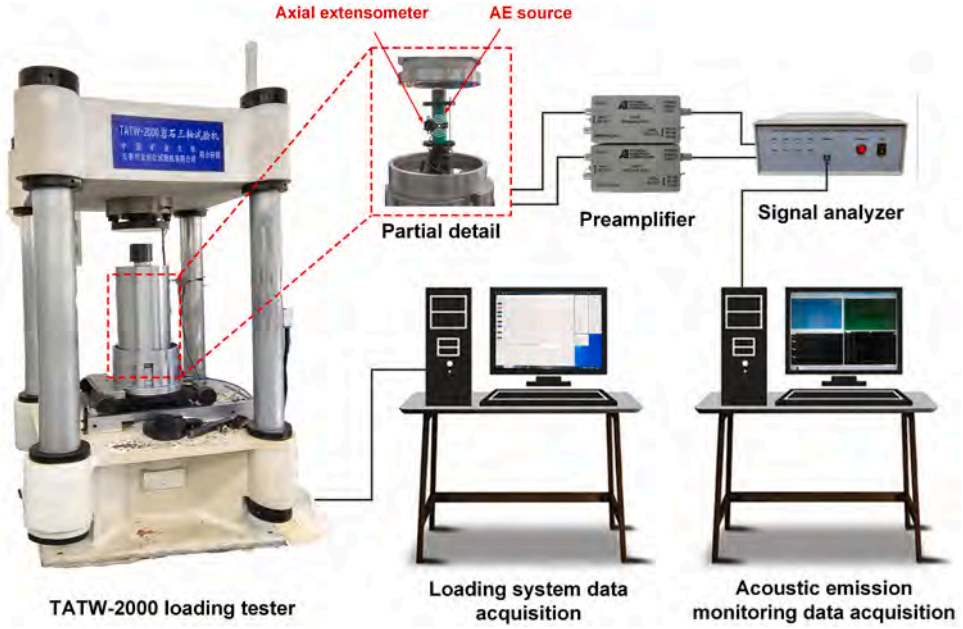

Fig. 3. Experimental setup for triaxial compression and AE monitoring.

For each combination of curing time and confining pressure, at least three specimens were tested to ensure repeatability of the mechanical response.

Prior to testing, each specimen was positioned on the loading pedestal, and a thin layer of petroleum jelly was applied to the end surfaces to reduce frictional effects. After assembling the triaxial cell, the confining pressure was applied at a constant rate of 0.1 MPa/s until the target value was reached and subsequently maintained throughout the test. Axial loading was then applied under displacement control at a constant rate of 0.5 mm/min until post-peak softening was clearly observed. During the entire loading process, axial load, axial displacement, and confining pressure were continuously recorded by the data acquisition system.

The complete stress–strain response, including the stable hardening stage, peak stress, and post-peak softening region, was used for subsequent constitutive analysis and post-failure characterization.

2.3.2. Acoustic emission monitoring

Acoustic emission (AE) monitoring was performed synchronously with the triaxial compression tests using an eight-channel DS5 AE acquisition system, as shown in Fig. 3. Four miniature AE sensors were mounted directly on the specimen surface at mid-height prior to installation in the triaxial cell. High-vacuum grease was used as a coupling agent, and the sensors were secured using heat-shrink tubing to ensure stable signal transmission throughout the loading process.

The AE preamplifier gain was set to 40 dB, and the signal acquisition threshold was fixed at 45 mV to effectively filter out environmental and mechanical noise during the loading process. AE waveforms were continuously recorded, and standard signal processing was applied to extract event-based parameters. In this study, AE analysis focused on the dynamic fractal characteristics of damage evolution via the b-value. The b-value was calculated based on the Gutenberg-Richter law ($log\ _{10}N = a - bA_{dB}$), where A_{dB} is the peak amplitude. To capture the real-time temporal evolution of damage, a sliding window method was employed with a window size of 200 events and a step size of 50 events. This statistical approach ensures sufficient data points for stable least-squares fitting while maintaining temporal resolution. Physically, the b-value serves as a scaling index of the fracture network: a high b-value indicates a dominance of small-scale, distributed micro-cracks (stable fracture), whereas a sharp decrease implies the nucleation and coalescence of large-scale macro-fractures (unstable failure).

2.3.3. Microstructural analysis

The microstructural morphology of the loess–slag backfill was examined using a VEGA 3 SBU scanning electron microscope (SEM) operated at an accelerating voltage of 20 kV. Two categories of samples were prepared for SEM observation: (i) fragments extracted from intact specimens at different curing times to investigate matrix evolution, and (ii) fragments collected from representative fracture regions of failed specimens to examine post-failure features.

All samples were freeze-dried to remove moisture while preserving microstructural integrity and subsequently coated with a thin gold layer to ensure electrical conductivity. To minimize sampling bias, a systematic random sampling strategy was adopted. Each specimen surface was first divided into a grid under low magnification, and several regions were randomly selected for high-magnification observation. The SEM images presented in this study are representative of the typical morphologies observed across these regions. The minimum b-value (b_{min}) was identified over the loading interval preceding peak stress to characterize the critical damage scaling state.

2.3.4. Mercury intrusion porosimetry analysis

Mercury intrusion porosimetry (MIP) was employed to quantitatively characterize the pore structure of the backfill material using a PoreMaster GT-60 porosimeter. MIP tests were performed on both intact specimens at different curing times and post-failure specimens subjected to various confining pressures. Representative samples with volumes of approximately 1–2 cm^3 were extracted from the specimen interior. For post-failure specimens, samples were deliberately extracted from the immediate vicinity of the macroscopic shear bands (fracture process zone). It is explicitly noted that these measurements represent the localized material degradation within the failure zone, rather than the average volumetric properties of the relatively intact bulk material.

Prior to testing, all samples were freeze-dried to eliminate moisture effects. The intrusion pressure ranged from atmospheric pressure up to 414 MPa, allowing the characterization of pore diameters spanning approximately 3 nm to 360 μm. From the MIP data, pore size distributions and cumulative intrusion volumes were obtained.

Fractal analysis of the pore structure was conducted using a thermodynamic fractal model based on the relationship between cumulative intrusion work and pore geometry. Log–log linear regression was applied to determine the fractal dimension of the intact pore structure (D_{f0}) and the post-failure pore structure (D_f). These fractal descriptors were subsequently used to interpret stiffness development, damage evolution, and post-peak softening behavior.

2.3.5. Constitutive fitting and post-peak parameter extraction

The fractional-order constitutive relation was calibrated against the experimental stress–strain curves using nonlinear regression techniques. To ensure physical validity, model fitting was strictly restricted to the stable hardening regime prior to peak stress. The fitting procedure yielded the generalized stiffness coefficient $\mathbb{K}$ and the fractional order α for each experimental condition.

Post-peak behavior was characterized using a softening index and a brittleness-related parameter derived from the descending branch of the stress–strain curves. These parameters were extracted for comparative analysis of post-peak stability rather than for constitutive prediction. All fitted parameters are summarized in Table 2. The fitting strategy was adopted to extract intrinsic rheological parameters rather than to reproduce the complete failure process.

3. Results and discussion

3.1. Macroscopic mechanical behavior

3.1.1. Stress-strain characteristics

The stress–strain response of the loess–slag backfill under different curing times and confining pressures is shown in Fig. 4. All curves

Table 2
Calibrated parameters of the fractional-order constitutive model under various curing times and confining pressures.

Curing days	Confining Pressure, σ_3 (MPa)	Generalized Stiffness, $\mathbb{K}$ (GPa)	Fractional Order, α	Fitting Quality, R^2	Post-peak softening stiffness, H (GPa)
1	0	1.274	0.192	0.999	−0.775
	2	1.419	0.207	0.977	−0.309
	4	1.661	0.363	0.921	−0.170
	6	1.724	0.419	0.998	−0.042
7	0	2.414	0.021	0.948	−2.342
	2	2.797	0.133	0.999	−0.412
	4	3.020	0.137	0.997	−0.180
	6	2.895	0.212	0.989	−0.085
14	0	3.543	0.080	0.997	−3.568
	2	3.329	0.091	0.992	−0.552
	4	3.725	0.126	0.995	−0.207
	6	4.019	0.103	0.999	−0.113
28	0	3.808	0.011	0.915	−4.746
	2	4.244	0.019	0.998	−0.771
	4	3.847	0.074	0.992	−0.265
	6	4.496	0.160	0.987	−0.134

Note: The fitting range is restricted to the stable hardening stage ($0 < \sigma \leq \sigma_{cd}$) to ensure physical validity.

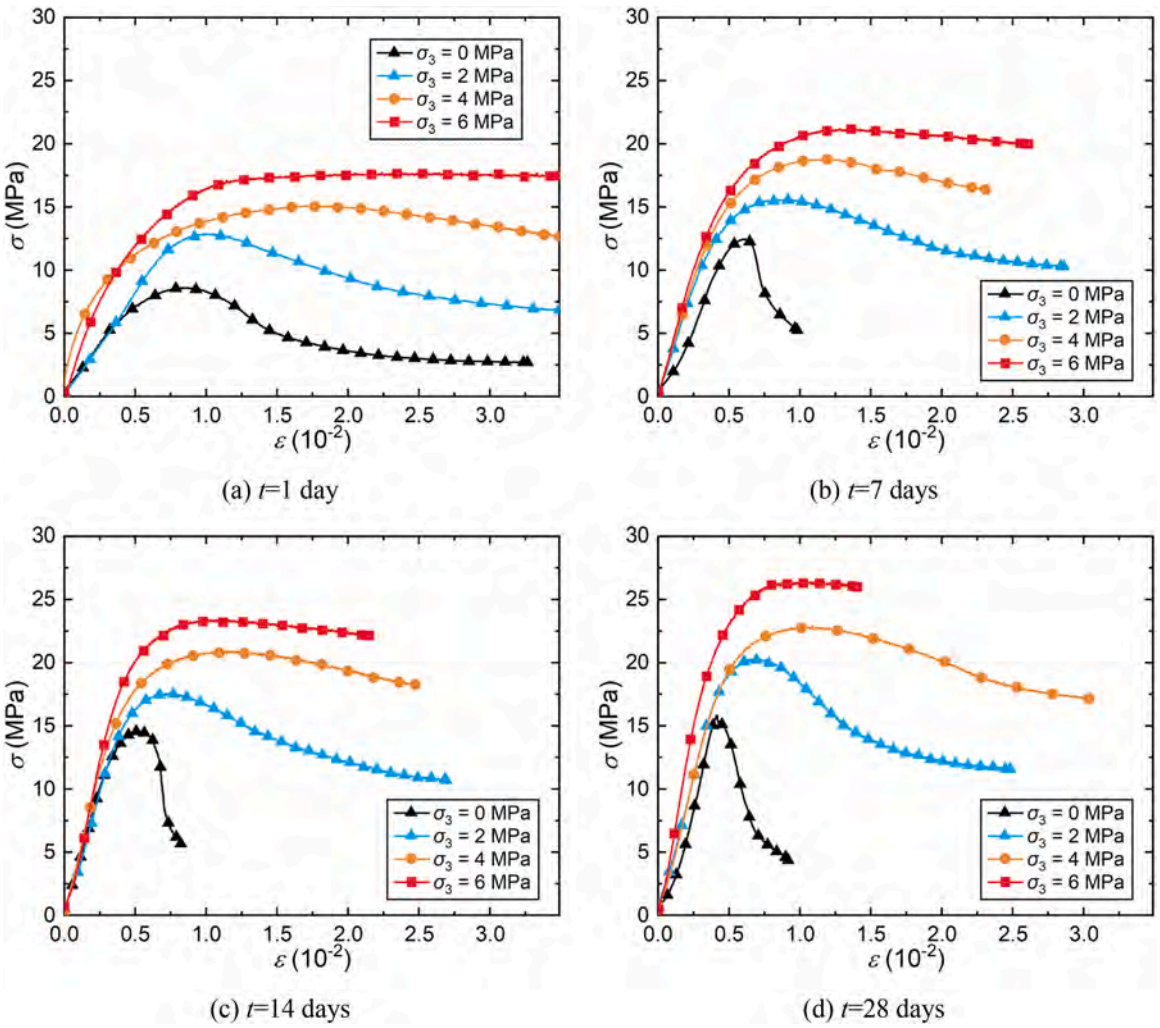

Fig. 4. Stress-strain curves under various curing times and confining pressures.

exhibit a typical four-stage behavior, including initial compaction, quasi-linear elasticity, strain hardening and post-peak softening. At low confining pressure (σ_3 = 0 MPa), the specimens show a pronounced brittle response: the stress increases rapidly to the peak value σ_c and then drops sharply with only a small amount of additional strain. With increasing confining pressure, both the initial tangent stiffness and the peak strength are enhanced, while the post-peak branch becomes much more gradual, indicating a clear transition from abrupt brittle failure to ductile strain-softening. Mechanistically, this transition occurs because high confining pressure effectively suppresses the propagation of tensile wing cracks (splitting) and enhances the frictional resistance among particles. Consequently, the failure mode shifts from localized brittle fracture to distributed shear deformation, which dissipates more energy and manifests as macroscopic ductility.

Curing time also has a significant effect on the shape of the curves. From 1 to 28 days, the peak stress and the strain at peak both increase, and the pre-peak portion becomes smoother and more extended. This reflects the progressive geopolymerization and microstructural densification of the loess–slag matrix, which improve the load-carrying capacity and delay the onset of unstable fracture. Under high confinement (σ_3 = 4–6 MPa) and longer curing times, the descending branch after the peak is approximately linear over a wide strain range. This nearly linear softening behavior enables the post-peak response to be characterized by a single softening stiffness parameter, defined as the average slope of the stress reduction with respect to strain, which provides a convenient scalar index for comparing ductility under different curing and confinement conditions.

3.1.2. *Strength evolution with curing time and confining pressure*

The coupled effects of curing time t and confining pressure σ_3 on the peak compressive strength σ_c are summarized in Fig. 5. As shown in Fig. 5(a), under each confining pressure level, σ_c increases monotonically with curing time following a typical exponential growth trend and gradually approaches a stable long-term strength limit. The fitted relations exhibit excellent correlation coefficients ($R^2 > 0.98$), indicating that the evolution of compressive strength is governed by reaction-controlled kinetics associated with ongoing geopolymerization and microstructural densification of the loess–slag matrix. The rapid strength gain observed during the early times (1–7 days) is primarily attributed to the formation of initial binding phases and pore refinement, whereas the subsequent slower growth stage reflects the gradual completion of gel development and structural stabilization.

Fig. 5(b) highlights the effect of confinement on peak strength at different curing times. For a given curing time, σ_c exhibits an approximately linear increase with σ_3, indicating that confining pressure effectively mobilizes frictional resistance and interparticle interlocking within the cemented granular skeleton, thereby suppressing tensile splitting and promoting shear-dominated load transfer. This linear strengthening trend remains evident even for the extrapolated long-term strength, confirming that confinement plays a consistent role in enhancing the ultimate load-bearing capacity of the backfill material [46,47]

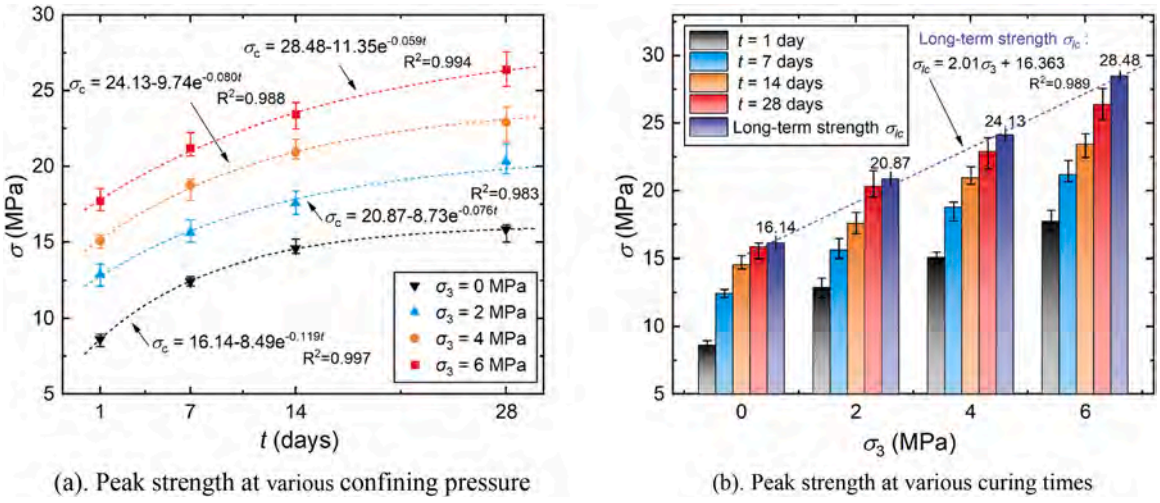

Fig. 5. Effects of curing time (t) and confining pressure (σ_3) on the triaxial compressive strength behavior (Error bars represent the standard deviation of three parallel specimens).

Taken together, Fig. 5 demonstrates that the macroscopic strength of the backfill is controlled by two synergistic mechanisms: curing time regulates the intrinsic strength potential through microstructural consolidation and gel network development, whereas confining pressure governs the efficiency of mobilizing this intrinsic strength via mechanical confinement and dilatancy suppression. This dual mechanism provides the macroscopic basis for the subsequent microstructural and fractal analyses, which aim to establish quantitative links between pore-network evolution and the observed strength enhancement behaviors.

3.2. Acoustic emission characteristics and determination of the crack-damage threshold

3.2.1. Spatiotemporal evolution and failure mode transition

Fig. 6 shows the coupled evolution of axial stress, AE ring-down counts and cumulative AE activity under representative curing times and confining pressures. In Fig. 6(a) and (b), the confining pressure is fixed at $\sigma_3 = 2$ MPa while the curing time increases from 1 to 28 days. In Fig. 6(c) and (d), the curing time is kept at 7 days while σ_3 varies from 0 to 6 MPa. At the initial and mid-elastic stages, AE activity remains low and sparse in all cases, indicating that deformation is dominated by pore closure and elastic adjustment of the cemented matrix.

As loading progresses, the cumulative AE curve in Fig. 6 (a–d) exhibits a clear inflection point, after which the accumulation rate increases rapidly. This blue-marked inflection point is defined as the crack-damage stress σ_{cd}. Physically, σ_{cd} is the stress level at which the specimen departs from the stable elastic–microcracking regime and enters a stage of accelerated damage coalescence. Mathematically, this corresponds to the stress level where the second derivative of the cumulative AE energy with respect to time becomes positive and sustained. Before σ_{cd}, the material response is essentially elastic at the macroscopic scale. Under higher confinement (e.g., Fig. 6(d), $\sigma_3 = 6$ MPa), the axial stress–strain curve develops an extended quasi-elastic region with a viscous-like transition, so the elastic limit cannot be clearly identified from the stress–strain curve alone. In such cases, the inflection point of the cumulative AE curve provides an objective and reproducible segmentation criterion between stable hardening and the onset of unstable damage.

The macroscopic failure photographs inserted in Fig. 6 further confirm this interpretation. At low confinement (e.g., Fig. 6(c)), the specimens exhibit axial splitting with open tensile cracks, consistent with the relatively abrupt post-peak stress drop. Under higher confinement (Fig. 6(d)), the failure mode changes to inclined shear bands with noticeable barreling, and the post-peak response becomes more gradual. This evolution is also captured by the RA–AF density heatmaps in the right column of Fig. 6. At low σ_3 and short curing time, the density concentrates above the RA/AF = 1 line and at high AF values, indicating a dominance of tensile-type AE signals. With increasing curing time or confining pressure, the density progressively shifts toward the RA-dominated region below the RA/AF = 1 line, and the proportion of shear-type events increases, reflecting the transition from tensile splitting to shear-controlled failure.

The evolution of σ_{cd} with curing time and confining pressure is summarized in Fig. 7. σ_{cd} increases with curing time following an exponential trend and increases approximately linearly with σ_3, consistent with the strengthening effects observed in Fig. 4 and Fig. 5. More importantly, the ratio σ_{cd} / σ_c remains highly stable at about 80–85 % for all conditions, with only small variance. This statistical consistency indicates that σ_{cd} is an intrinsic damage-transition point linked to the overall failure process of the backfill, rather than a test-dependent artifact. Therefore, σ_{cd} can be used as a reliable mechanical boundary between the pre-peak constitutive regime and the onset of damage localization.

3.2.2. Fractal evolution of damage revealed by b-value

To further quantify the dynamic evolution of damage, the frequency–magnitude distribution of AE events was analyzed using the Gutenberg–Richter type relationship. For each loading stage, the cumulative number of AE events with amplitude greater than A follows

$$\log_{10} N(>A) = a - bA_{dB} \tag{1}$$

where $N(>A)$ is the number of events with amplitude larger than A, a is a constant related to the overall activity level, and b is the b-value obtained from the slope of the best-fit line, i.e.,

$$b = -\frac{\partial \log_{10} N(>A_{dB})}{\partial A_{dB}} \tag{2}$$

In this study, the b-value is treated as a dynamic fractal index of the damage network: lower b indicates a broader distribution of high-energy events and a higher degree of localization, whereas higher b corresponds to more uniformly distributed, small-scale cracking.

The evolution of b-value with axial strain for representative conditions is shown in Fig. 8 (a–d). A consistent three-stage pattern can be identified in all cases. At the initial stage, the b-value decreases rapidly as small, randomly distributed microcracks evolve into a population containing more high-energy events. As the stress approaches σ_{cd}, the b-value reaches a minimum b_{min}, marking the onset of unstable crack coalescence. Beyond σ_{cd} and up to the peak stress σ_c, the b-value tends to

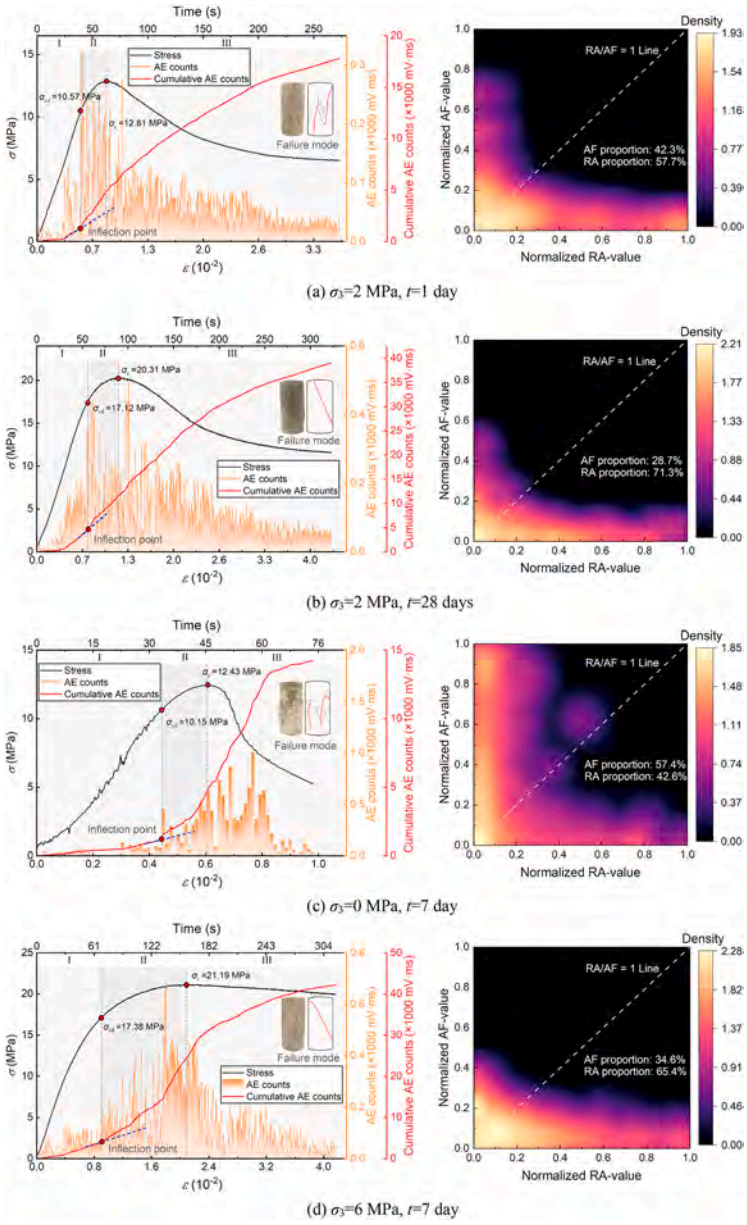

Fig. 6. Coupled evolution of AE damage characteristics and failure mechanisms under different conditions: (Left column) AE counts and cumulative energy superimposed on stress-strain curves; (Right column) RA-AF density heatmaps.

rebound slightly or remain at a quasi-steady level, indicating that damage progressively transitions from tensile microcracking to frictional sliding and shear-band development.

The effect of curing time can be seen by comparing Fig. 8(a) and Fig. 8(b), where the confining pressure is fixed at $\sigma_3 = 2$ MPa. For the 1-day specimen, the immature microstructure provides limited resistance to crack growth, and the b-value drops sharply to a moderate minimum of $b_{min} \approx 1.07$. After 28 days of curing, the loess–slag matrix becomes denser and better cemented, leading to a more gradual decrease of b-value and a lower minimum $b_{min} \approx 0.76$. This indicates that under the same confinement, the mature matrix allows microcracks to accumulate more energy before localization, and the damage process is less dominated by extreme events.

The influence of confinement is more pronounced, as illustrated in Fig. 8(c) and Fig. 8(d) for specimens cured for 7 days. At zero confinement (Fig. 8(c), $\sigma_3 = 0$ MPa), the b-value experiences a dramatic drop to $b_{min} \approx 0.63$, implying a strong concentration of large-energy AE events and highly localized tensile splitting. Under high confinement (Fig. 8(d), $\sigma_3 = 6$ MPa), the minimum b-value increases to about $b_{min} \approx 1.13$, and its evolution curve becomes much flatter. This behavior reflects the confinement-induced suppression of tensile crack opening and the promotion of distributed shear deformation along multiple bands, rather than the formation of a single dominant fracture plane.

Overall, the b-value analysis reveals a clear link between damage fractality and macroscopic ductility. Low b_{min}values (e.g., $b_{min} < 1.0$) correspond to catastrophic, brittle damage with strongly localized crack paths, while higher b_{min}values (around or above 1.0) indicate a more fragmented and spatially distributed damage network that can accommodate deformation in a ductile manner. Combined with the evolution of σ_{cd} in Fig. 7, these results demonstrate that curing-induced microstructural consolidation and confinement-induced suppression of tensile cracking jointly control the dynamic fractal characteristics of the damage process, and thereby govern the transition from brittle splitting to ductile shear failure in the loess–slag backfill.

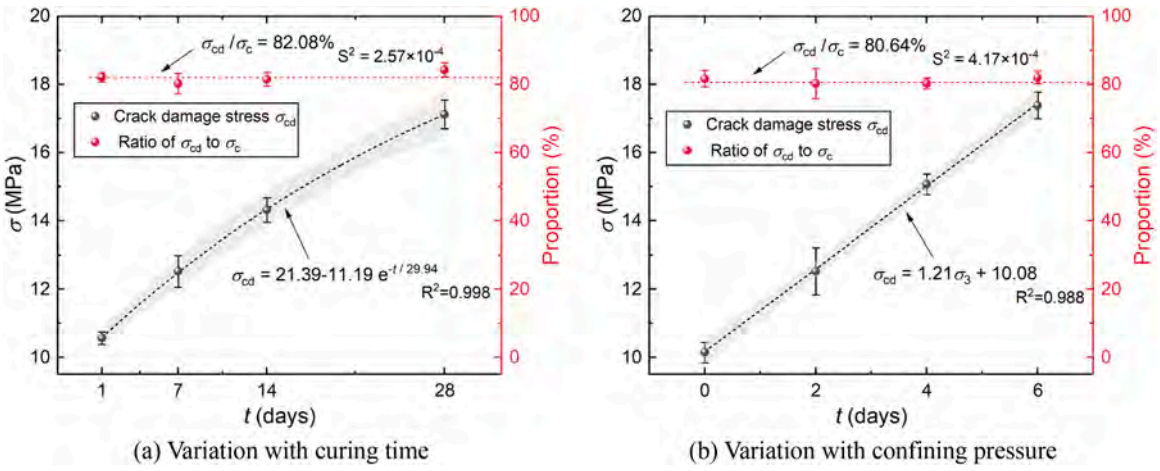

Fig. 7. Evolution of crack damage stress (σ_{cd}) and the ratio of damage threshold to peak strength (σ_{cd} / σ_c).

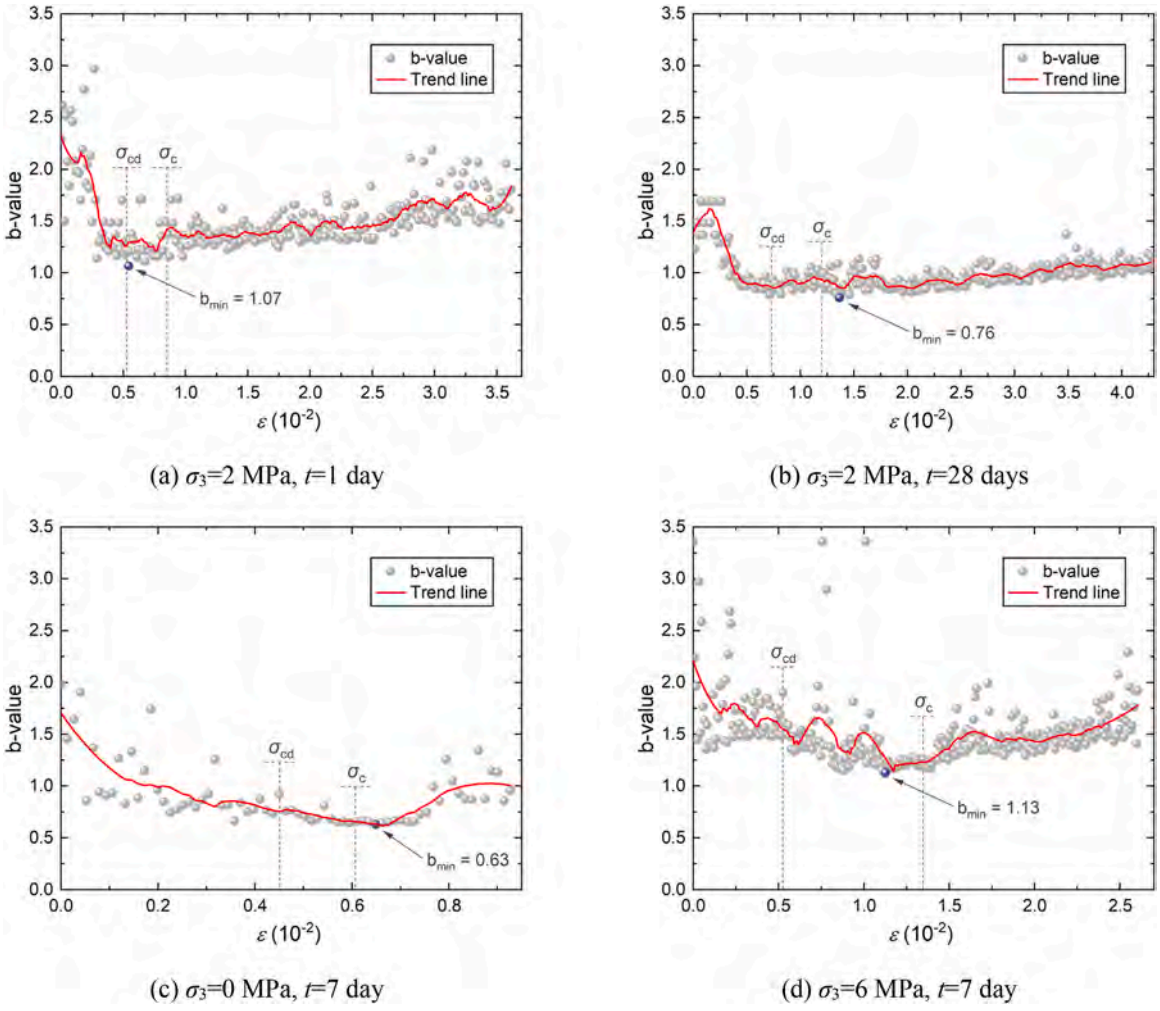

Fig. 8. Fractal dimension evolution of damage (b-value).

3.3. Microstructural morphology

3.3.1. Densification of initial matrix structure

The SEM images in Fig. 9 provide direct microstructural evidence for the curing- and confinement-dependent mechanical behavior. At early curing time (Fig. 9(a), t = 1d), the matrix exhibits a heterogeneous and weakly bonded structure. Loess agglomerates remain porous, unreacted slag particles are embedded within an incompletely polymerized gel network, and microcracks are widely distributed along interparticle contacts. This immature matrix explains the rapid AE activation and relatively low crack-damage stress observed in Fig. 6(a).

With extended curing (Fig. 9(b), t = 28d), the hydration/geopolymer reaction produces a markedly denser and more homogeneous matrix. The pore structure becomes refined, microcracks are largely

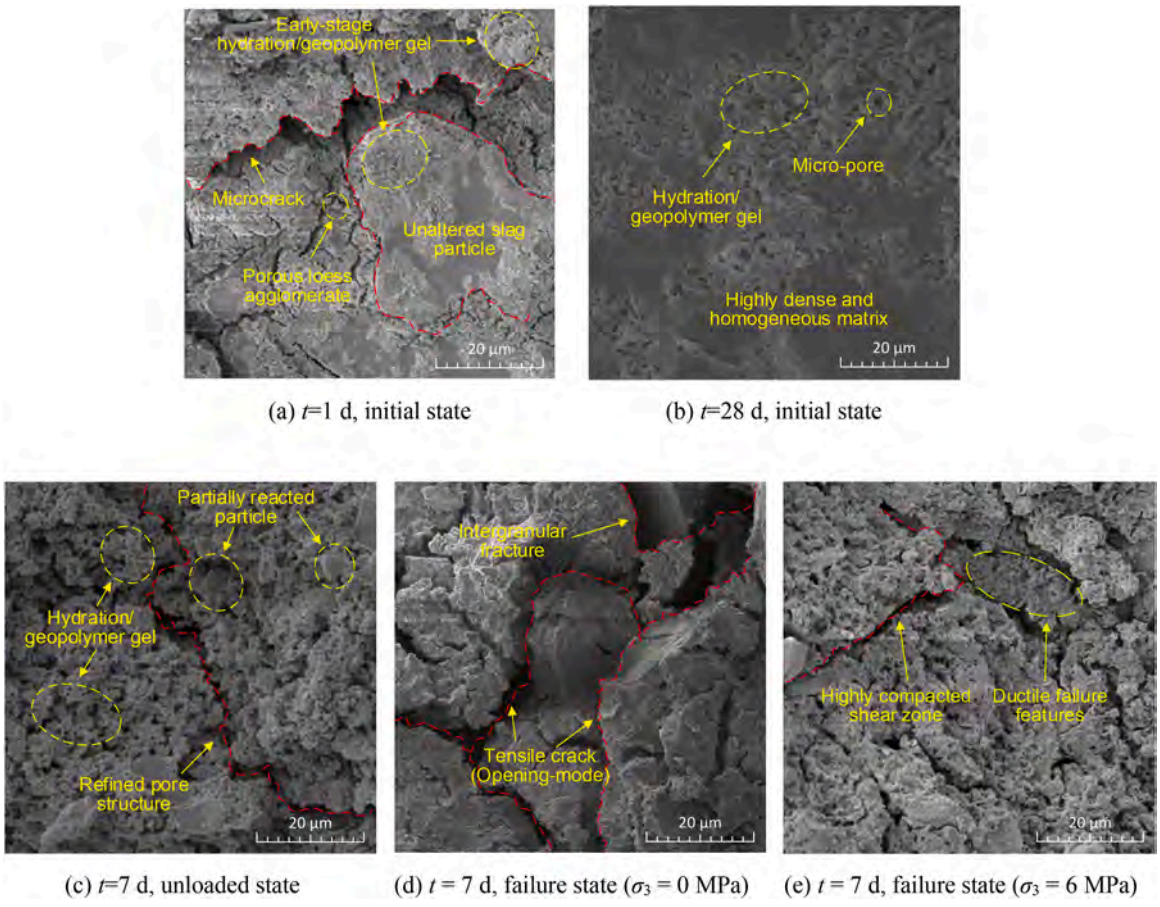

Fig. 9. Microstructural evolution with curing time and confining pressure.

healed or bridged by the polymerized gel, and the interfaces between slag particles and surrounding gel appear continuous and well bonded. This microstructural consolidation increases both the elastic stiffness and the resistance to microcrack coalescence, consistent with the elevated peak strength and higher σ_{cd} values observed in Fig. 7.

3.3.2. *Transition of failure mechanisms under confinement*

Fig. 9 (c–e) focuses on specimens with the same curing time of 7 days but different confinement conditions after triaxial loading. Fig. 9(c) shows a region away from the main failure plane, where the microstructure is only weakly affected by loading. Hydration gel has formed a relatively continuous skeleton, and the pore structure is already refined compared with the 1 d state, but the matrix still contains partially reacted particles and residual micro-pores. This microstructure represents the baseline condition at $t = 7$d against which the confined failure patterns in Fig. 9(d) and (e) can be compared.

The influence of confinement on microcrack propagation is evident in the failure-state images. At zero confinement (Fig. 9(d)), the failure surface is dominated by intergranular tensile cracks, consistent with the low b_{min} values and tensile-dominated RA–AF signatures observed in Fig. 6(c) and Fig. 8(c). Under high confinement (Fig. 9(e), $\sigma_3 = 6$MPa), the microstructure near the failure plane becomes highly compacted, and shear bands with ductile smearing are clearly observable. The gel matrix displays local crushing and shear-driven particle rearrangement rather than open-mode cracking. This shear-dominated pattern agrees with the higher b_{min} values in Fig. 8(d) and the shift toward RA-dominated AE signals in Fig. 6(d).

Overall, Fig. 9 demonstrates that curing time primarily controls the intrinsic bonding quality and pore refinement of the loess–slag matrix, whereas confining pressure governs the micromechanical mode of crack propagation during failure. The transition from porous, crack-prone early-age microstructure to a dense, well-bonded matrix provides the basis for the observed increase in σ_{cd}, peak strength, and post-peak softening behavior. Meanwhile, the confinement-induced switch from tensile splitting to shear-band formation explains the evolution of AE characteristics and fractal damage signatures. These microstructural observations serve as the physical foundation for the fractal interpretation of damage and the constitutive modeling.

3.4. *Pore structure characterization by MIP*

3.4.1. *Evolution of pore structure with curing time*

Mercury intrusion porosimetry (MIP) provides a quantitative description of the pore network and forms the basis for evaluating the static fractal dimension D_{f0}. The pore size distribution (PSD) at different curing times is shown in Fig. 10(a). At $t = 1$day, the PSD is dominated by a broad peak in the harmful capillary pore range (>1000 nm), representing loosely packed voids among unreacted loess agglomerates and slag particles. As curing progresses, this macropore peak gradually decreases in intensity and shifts toward the refined pore region (<50 nm) [48–50]. By $t = 28$days, the refined-pore fraction increases substantially, indicating that hydration/geopolymer gels (C–S–H and N–A–S–H) have filled and subdivided the initially large interconnected capillaries into smaller, more isolated pores. This left-shift and flattening of the PSD directly reflects the space-filling action of the reaction products.

The cumulative pore volume curves in Fig. 10(b) further confirm this densification process. The total intruded volume decreases monotonically with curing time, and the reduction is most pronounced within the first 7 days, corresponding to the high reaction rate of the geopolymerization process. As the matrix becomes denser and diffusion

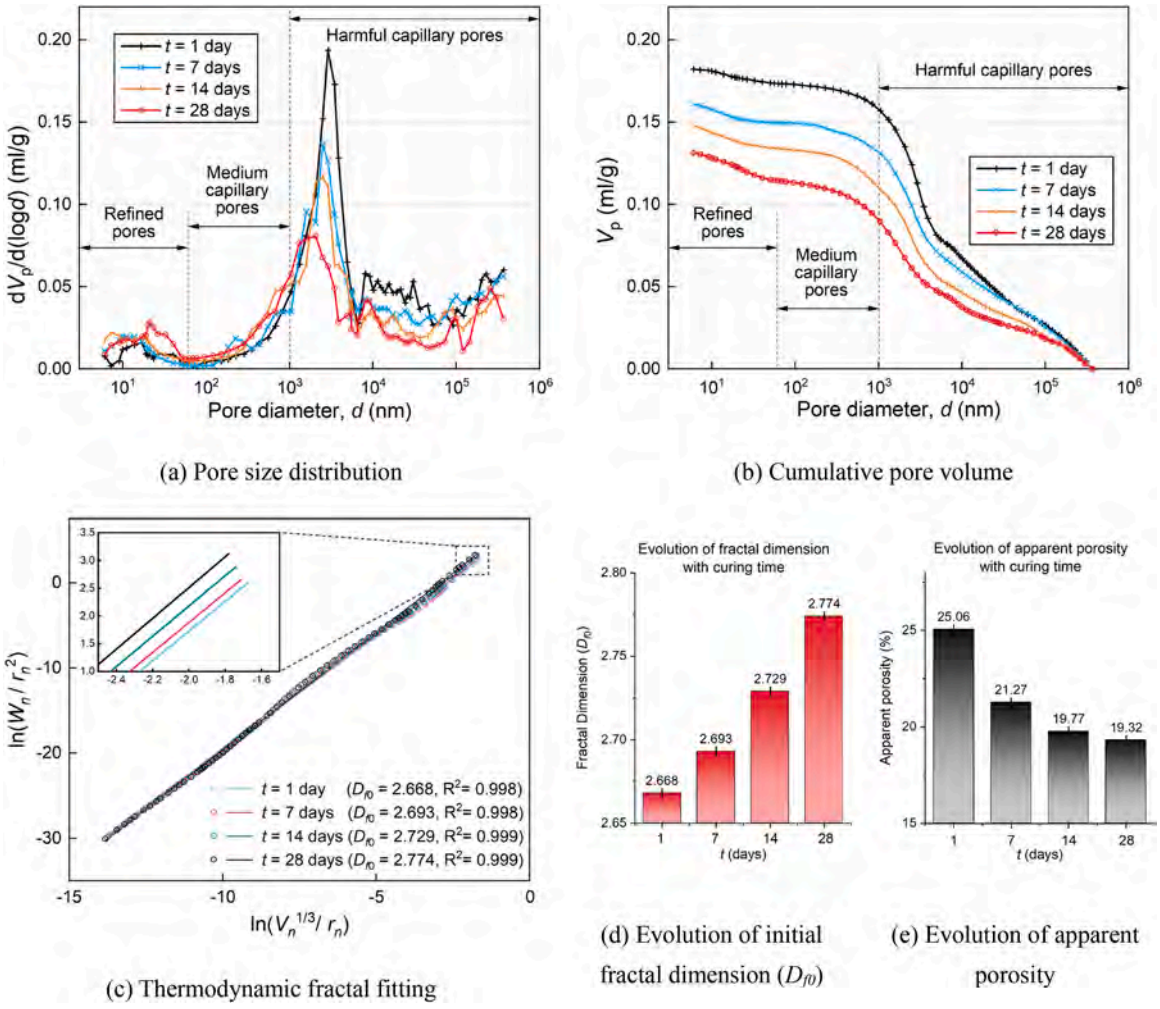

Fig. 10. Effect of curing time on initial pore structure (MIP analysis).

paths are progressively blocked, the rate of pore-volume reduction slows down. The apparent porosity summarized in Fig. 10(e) drops from 25.06 % at 1 day to 19.32 % at 28 days, showing that a substantial portion of the initial void space is converted into solid skeleton.

While porosity and PSD capture the volumetric aspects of the pore network, they do not fully describe its morphological complexity. To characterize the topology of the pore system, the thermodynamic fractal model is applied to the MIP data. As shown in Fig. 10(c), the double-logarithmic plots of $\ln\left(W_n/r_n^2\right)$ versus $\ln\left(V_n^{1/3}/r_n\right)$ exhibit excellent linearity over the entire intrusion range for all curing times, with correlation coefficients $R^2 > 0.998$. According to the thermodynamic fractal relation

$$\ln\left(\frac{W_n}{r_n^2}\right) = (D_{f0} - 3)\ln\left(\frac{V_n^{1/3}}{r_n}\right) + C \tag{3}$$

the slope of these lines directly yields the initial fractal dimension D_{f0}, confirming that the pore network possesses pronounced self-similar characteristics. Although cementitious materials may theoretically exhibit multi-fractal behavior distinguishing between gel and capillary pores, the exceptionally high linearity ($R^2 > 0.998$) observed across the entire measurement range indicates that a single fractal dimension (D_{f0}) provides a statistically sufficient descriptor for the pore topology in this study. This global index effectively captures the overall space-filling capacity relevant to macroscopic stiffness, avoiding the over-parameterization associated with multi-fractal models.

The evolution of D_{f0} is presented in Fig. 10(d). Unlike the apparent porosity, which decreases with curing time, D_{f0} increases steadily from 2.668 at 1 day to 2.774 at 28 days. This increase indicates that the pore surfaces become more tortuous and the pore network becomes topologically more complex as gels deposit and subdivide the original voids. In physical terms, a higher D_{f0} corresponds to a more space-filling solid skeleton with enhanced topological connectivity. This complex microstructure provides denser stress transmission pathways and stronger inter-particle bonding, thereby offering greater resistance to elastic deformation and resulting in a higher generalized stiffness $\mathbb{K}$. This transition from a simple, low-D_{f0} porous framework to a dense, high-D_{f0} network is consistent with the observed increases in elastic modulus, peak strength and crack-damage stress σ_{cd}, demonstrating that D_{f0} is a sensitive microstructural indicator of curing-induced matrix strengthening.

3.4.2. *Impact of confining pressure on post-failure porosity*

Fig. 11 presents the mercury intrusion results for specimens subjected to different confining pressures after triaxial loading. Since all specimens share the same initial curing time, the differences reflect solely the influence of confinement on the damage-induced evolution of the pore network.

The pore size distribution in Fig. 11(a) shows that the specimen tested without confinement ($\sigma_3 = 0$ MPa) develops a pronounced new peak in the harmful capillary pore range (>10 μm). This represents the formation of large, open tensile cracks and the dilation of the matrix during brittle splitting. In contrast, when confinement is applied, the

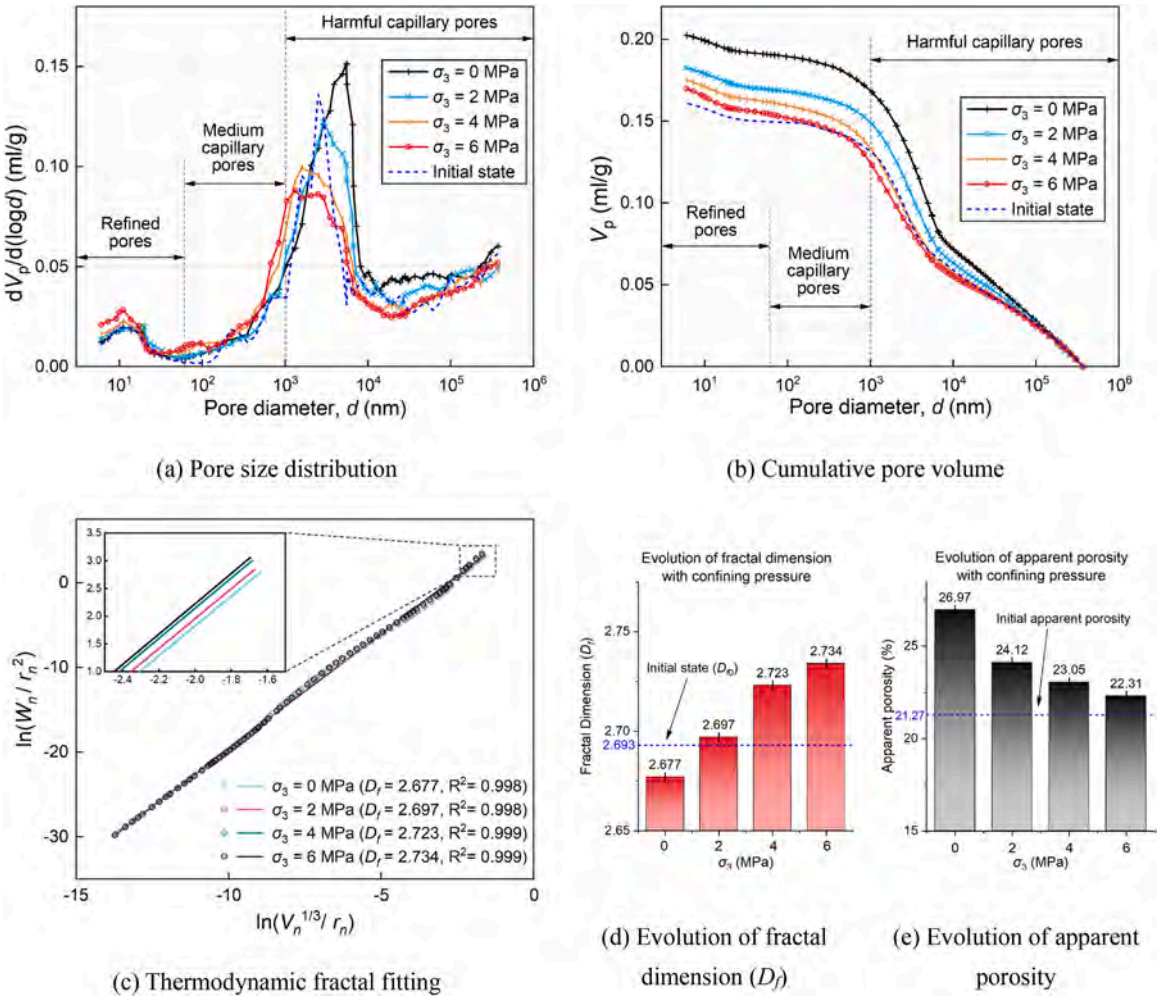

Fig. 11. Effect of confining pressure on post-damage pore structure (MIP analysis).

PSD curve retains a shape much closer to the intact state. At $\sigma_3 = 6$MPa, the macropore peak is largely suppressed, indicating that lateral pressure inhibits crack opening and restricts the formation of through-going voids.

The cumulative pore volume curves in Fig. 11(b) further illustrate this effect. The total intrusion volume of the unconfined specimen increases significantly due to the generation of extensive tensile cracks. As σ_3 increases, the intrusion volume increment becomes progressively smaller, implying that the deformation is accommodated mainly through the compaction of existing micro-pores rather than the creation of new macroscopic voids. This behavior is consistent with the shear-dominated failure modes observed in the SEM images of Fig. 9(e).

The apparent porosity values in Fig. 11(e) highlight the stabilizing effect of confinement. At $\sigma_3 = 0$MPa, the post-failure porosity rises to 26.97 %, exceeding the intact-state level and reflecting severe structural degradation. Under high confinement, the porosity is maintained near 22.31 %, only slightly above the initial value. This indicates that confinement suppresses volumetric dilation and limits the structural disruption associated with failure.

To characterize the topology of the residual fracture network, the thermodynamic fractal model is applied to the post-damage MIP curves. The linearity of the double-logarithmic fits in Fig. 11(c) confirms that the damaged pore networks still exhibit fractal characteristics. The resulting fractal dimensions shown in Fig. 11(d) increase from 2.677 at $\sigma_3 = 0$MPa to 2.734 at $\sigma_3 = 6$MPa. A lower fractal dimension at zero confinement indicates that the fracture network has evolved into relatively simple, low-dimensional planar cracks characteristic of brittle tensile failure. In contrast, the higher fractal dimensions under confinement reflect a more complex and tortuous damage structure formed by distributed shear bands, particle rearrangement and local pore collapse.

These results demonstrate that confining pressure fundamentally alters the residual pore structure by suppressing tensile crack opening and promoting a distributed shear-driven damage network. The preservation of higher post-damage fractal dimensions under confinement provides the structural basis for the improved ductility and residual strength observed in the mechanical response, linking the pore-scale topology to the macroscopic failure behavior.

4. Fractional-order constitutive modeling based on micro-fractal characterization

4.1. Fractional constitutive formulation

Under monotonic loading, the pre-damage response of the backfill exhibits clear non-linear hardening and memory effects, which cannot be captured by a simple linear elastic model. To account for this hereditary behavior, the stress–strain relation in the pre-damage regime is formulated using a fractional Abel element. In the time domain, the constitutive equation is written as

$$\sigma(t) = \eta_\alpha {}^{\mathrm{RL}}D_t^\alpha \varepsilon(t), 0 < \alpha < 1 \tag{4}$$

where η_α is the fractional material coefficient with the dimension of

generalized viscosity, and ${}^{\mathrm{RL}}D_t^{\alpha}(\cdot)$ denotes the Riemann–Liouville fractional derivative of order α, defined by

$$ {}^{\mathrm{RL}}D_t^{\alpha} f(t) = \frac{1}{\Gamma(1-\alpha)} \frac{\mathrm{d}}{\mathrm{d}t} \int_0^t \frac{f(\tau)}{(t-\tau)^{\alpha}} \mathrm{d}\tau, 0 < \alpha < 1 \tag{5} $$

This operator reflects that the current stress depends on the entire past history of strain through a power-law kernel.

For a power-law function $f(t) = t^m$with $m > -1$, the Riemann–Liouville derivative has the closed form

$$ {}^{\mathrm{RL}}D_t^{\alpha} t^m = \frac{\Gamma(m+1)}{\Gamma(m+1-\alpha)} t^{m-\alpha} \tag{6} $$

In the present triaxial tests, the axial strain is applied at a constant rate $\dot{\varepsilon}$, so that

$$ \varepsilon(t) = \dot{\varepsilon} t = \dot{\varepsilon} t^1 \tag{7} $$

Substituting this expression into the above property with $m = 1$ gives

$$ {}^{\mathrm{RL}}D_t^{\alpha} \varepsilon(t) = \dot{\varepsilon}\, {}^{\mathrm{RL}}D_t^{\alpha} t = \dot{\varepsilon} \frac{\Gamma(2)}{\Gamma(2-\alpha)} t^{1-\alpha} = \dot{\varepsilon} \frac{t^{1-\alpha}}{\Gamma(2-\alpha)} \tag{8} $$

because $\Gamma(2) = 1!$. The corresponding stress in the pre-damage regime is therefore

$$ \sigma(t) = \eta_{\alpha}\, {}^{\mathrm{RL}}D_t^{\alpha} \varepsilon(t) = \eta_{\alpha} \dot{\varepsilon} \frac{t^{1-\alpha}}{\Gamma(2-\alpha)} \tag{9} $$

Expressing the response in terms of strain rather than time, and using $\varepsilon = \dot{\varepsilon} t$ (hence $t = \varepsilon/\dot{\varepsilon}$), yields

$$ \sigma(\varepsilon) = \eta_{\alpha} \dot{\varepsilon} \frac{(\varepsilon/\dot{\varepsilon})^{1-\alpha}}{\Gamma(2-\alpha)} = \eta_{\alpha} \dot{\varepsilon}^{\alpha} \frac{\varepsilon^{1-\alpha}}{\Gamma(2-\alpha)} \tag{10} $$

Collecting the constant terms, a generalized stiffness coefficient $\mathbb{K}$ is introduced as

$$ \mathbb{K} = \frac{\eta_{\alpha} \dot{\varepsilon}^{\alpha}}{\Gamma(2-\alpha)} \tag{11} $$

so that the fractional stress–strain relation in the pre-damage domain takes the compact form

$$ \sigma(\varepsilon) = \mathbb{K} \varepsilon^{1-\alpha}, 0 < \alpha < 1 \tag{12} $$

In this expression, $\mathbb{K}$ represents the generalized stiffness of the fractional element under the prescribed strain rate, while α controls the degree of non-linearity between the purely elastic response ($\alpha \to 0$) and a more viscous-like behavior ($\alpha \to 1$). The capability of this fractional form to reproduce the pre-damage stress–strain response of the backfill is demonstrated by the representative fitting results shown in Fig. 12, where the model accurately captures the curvature and hardening trend within the $\sigma \le \sigma_{cd}$ regime. Subsequent sections identify $\mathbb{K}$ and α from experimental data and relate them to the fractal characteristics of the pore and damage networks. It should be noted that the fitting process excluded the initial non-linear compaction stage, as this phase is dominated by geometric void closure rather than the material's constitutive rheological behavior. Consequently, the specific fitting range was selected from the onset of linear elasticity (typically $\varepsilon \approx 0.1\%$) up to the peak stress (σ_{peak}), ensuring that the derived fractional order α accurately reflects the hardening mechanism.

The fractional constitutive form introduced in Eq. (12) is used here as a phenomenological description of the pre-damage response, motivated by two observed features: (i) the stress–strain curve before σ_{cd} exhibits stable non-linear hardening without stiffness loss, and (ii) the material shows clear hereditary behavior, indicating a path-dependent response. Within this regime, AE activity remains low and no localization develops, so the non-linearity can be represented by the fractional order without introducing an explicit damage variable.

The parameters $\mathbb{K}$ and α identified from the $\sigma \le \sigma_{\mathrm{cd}}$ domain are therefore state-dependent descriptors rather than universal material constants. $\mathbb{K}$ reflects the load-bearing capacity of the curing-dependent skeleton, while α captures the deviation from linear elasticity. Subsequent fractal analyses do not aim to derive these parameters from first principles, but rather to interpret how changes in pore topology and damage fractality are reflected in their values.

4.2. Determination of model parameters

The fractional constitutive model in Eq. (12) was calibrated using the axial stress–strain data within the pre-damage domain, which is bounded by the crack-damage stress σ_{cd}. This threshold corresponds to the inflection point of the cumulative AE activity, where the deformation mechanism begins to transition from stable hardening to damage-induced stiffness degradation. By restricting the fitting range to $0 < \sigma \le \sigma_{\mathrm{cd}}$, the extracted parameters reflect the intrinsic rheological behavior of the intact matrix rather than the influence of macroscopic crack coalescence. Representative fitting curves within this domain are shown in Fig. 12.

The model parameters $\mathbb{K}$ and α were obtained through non-linear regression of the fractional form against the experimental data for all curing–confinement combinations. Their variation across the 16 loading scenarios is summarized in Table 2, while Fig. 13 provides a visual illustration of the systematic trends. The stiffness-like parameter $\mathbb{K}$ increases consistently with curing time, whereas the fractional order α

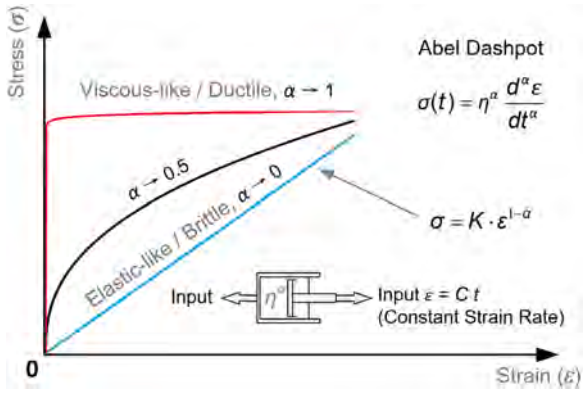

Fig. 12. Theoretical representation of the fractional-order constitutive model.

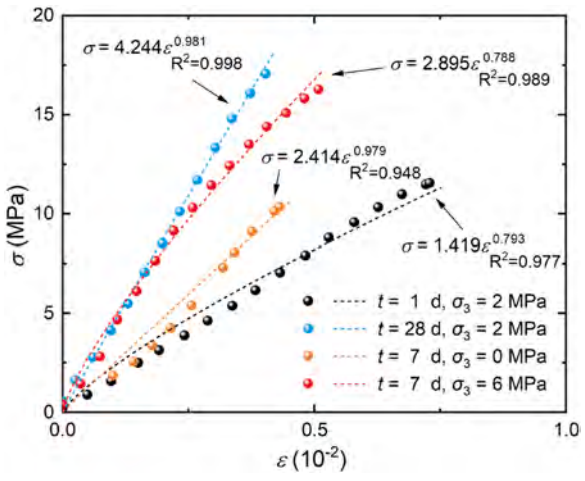

Fig. 13. Calibration of the fractional-order constitutive model against experimental stress-strain data.

varies with both curing and confining pressure, capturing the degree of non-linearity in the pre-damage response. All fittings exhibit high determination coefficients ($R^2 > 0.98$), confirming the stability and reproducibility of the calibration procedure.

These parameter sets form the basis for the subsequent analysis. In next section, their physical relevance is examined by establishing quantitative mappings with the fractal descriptors of pore structure (D_{f0}) and damage evolution ($b_{\min}$).

4.3. Physical interpretation and fractal mapping

4.3.1. Static fractal control on generalized stiffness ($\mathbb{K}$ vs. D_{f0})

The generalized stiffness $\mathbb{K}$ in the fractional model reflects the load-carrying capacity of the backfill skeleton in the pre-damage regime. The initial fractal dimension D_{f0} obtained from MIP quantifies the topological complexity and space-filling ability of the pore network before loading. It is therefore natural to examine whether the calibrated $\mathbb{K}$ correlates with the static fractal descriptor D_{f0}.

Fig. 14(a) plots $\mathbb{K}$ against D_{f0} for all curing times and confining pressures. A clear monotonic trend is observed: specimens with higher D_{f0} systematically exhibit larger $\mathbb{K}$. This indicates that as the pore structure evolves from a loose, low-D_{f0} state at early time to a dense, highly space-filling network at later time, the pre-damage stiffness of the material increases accordingly. To quantify this dependence, the following shifted exponential relation is adopted:

$$\mathbb{K}(D_{f0}) = \mathbb{K}_{\min} + \Delta\mathbb{K}\left[1 - \exp\left(-\lambda(D_{f0} - D_{f0,\min})\right)\right] \tag{13}$$

where $D_{f0,\min}$ is the minimum fractal dimension at 1 day curing, $\mathbb{K}_{\min}$ represents the baseline stiffness at this reference state, $\mathbb{K}_{\min} + \Delta\mathbb{K}$ denotes the asymptotic stiffness corresponding to a highly densified matrix, and λ is a sensitivity coefficient that controls how rapidly $\mathbb{K}$ approaches its upper bound as D_{f0} increases.

This functional form has a straightforward physical interpretation for the loess–slag backfill. When D_{f0} is close to $D_{f0,\min}$, the pore network is dominated by large capillary pores and weak interparticle contacts, so $\mathbb{K}$ remains near $\mathbb{K}_{\min}$. As hydration products progressively fill and subdivide these pores, even a modest increase in D_{f0} leads to a rapid rise in $\mathbb{K}$, reflecting the formation of a continuous, space-filling load-bearing skeleton. Once D_{f0} approaches its upper range, most macropores have already been transformed into refined gel pores and the available room for further stiffness gain becomes limited, causing $\mathbb{K}$ to asymptotically approach $\mathbb{K}_{\min} + \Delta\mathbb{K}$. The high correlation obtained in Fig. 14(a) therefore supports the view that the static fractal dimension D_{f0} is a key microstructural indicator governing the generalized stiffness in the fractional constitutive response.

4.3.2. Dynamic fractal control on fractional order (α vs. b_{min})

While $\mathbb{K}$ is primarily controlled by the initial pore structure, the fractional order αcharacterizes the shape of the pre-damage stress–strain curve, i.e., the degree of non-linearity between purely elastic and more viscous-like hardening. This dynamic feature is closely related to how microcracks of different sizes are activated and distributed during loading.

The minimum AE b-value $b_{\min}$ serves as a compact indicator of the relative proportion of large- and small-energy events at the critical damage state. A lower $b_{\min}$ implies that large events dominate, corresponding to highly localized cracking, whereas a higher $b_{\min}$ indicates a more even distribution of event sizes and hence more distributed damage. Fig. 14(b) presents the relationship between α and $b_{\min}$ for all tested conditions. The data points align well along a straight line, which can be expressed as

$$\alpha = p\, b_{\min} + q \tag{14}$$

where $p > 0$ is the regression slope and q is the intercept determined from the experimental dataset.

This linear mapping provides a physically meaningful interpretation of the fractional order. In the brittle regime, where $b_{\min}$ falls to relatively low values, the damage process is dominated by a few large events and rapidly localized cracks. In this case, the fitted α approaches small values, and the stress–strain response becomes nearly linear up to the point of sudden failure. Conversely, in the ductile regime promoted by higher confinement and longer curing, $b_{\min}$ increases, indicating that microcracks are more uniformly distributed across scales and that energy is dissipated through a large number of moderate events. The corresponding α values become larger, and the pre-damage stress–strain curve exhibits pronounced non-linearity and pseudo-viscous hardening.

This behavior is consistent with the microstructural and post-failure fractal observations. Specimens with larger αunder high confining pressure maintain a complex, tortuous fracture network with higher post-damage fractal dimension, as revealed by MIP analysis. In contrast, specimens with small α and low $b_{\min}$tend to develop simplified planar cracks and reduced structural complexity after failure. Although the α–$b_{\min}$ relation is established empirically, its monotonic and physically interpretable nature suggests that the fractional order can be viewed as a macroscopic index reflecting the dynamic fractal characteristics of damage evolution.

Overall, the mappings indicate that $\mathbb{K}$ reflects the static fractal topology of the pore skeleton, whereas αencodes the dynamic scaling characteristics of damage evolution captured by $b_{\min}$. These relations

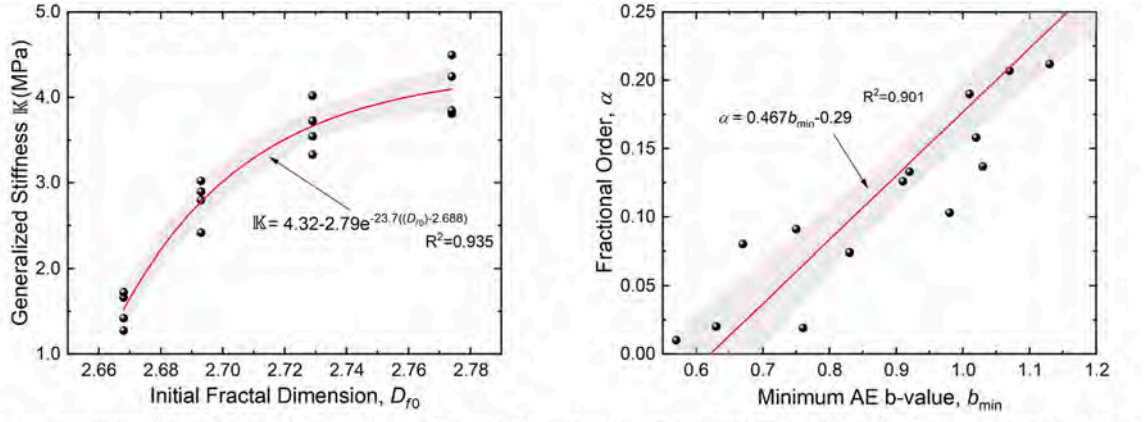

(a) exponential dependence of generalized stiffness ($\mathbb{K}$) on the initial pore fractal dimension (D_{f0})

(b) linear correlation between the fractional order (α) and the minimum AE b-value ($b_{\min}$).

Fig. 14. Physical mapping between macroscopic constitutive parameters and microscopic fractal characteristics.

provide a coherent micro-to-macro interpretation of the fractional parameters and form a consistent basis for describing both pre-damage behavior and subsequent softening.

4.4. Peak-softening characterization based on damage-induced fractal increment

The post-peak regime reflects the macroscopic instability after stress localization and crack coalescence, where the load-bearing skeleton undergoes progressive degradation. In the present experiments, the post-peak response is quantified using a softening parameter extracted from the descending branch of the stress–strain curve and is further normalized to enable comparison across different curing times and confining pressures.

The post-peak stress–strain relation is described using an exponential softening form,

$$\sigma(\varepsilon) = \sigma_c \exp[H(\varepsilon - \varepsilon_c)], \varepsilon \geq \varepsilon_c \tag{15}$$

where σ_c and $\varepsilon_c$denote the peak stress and peak strain, respectively, and $H < 0$ characterizes the post-peak softening rate. A more negative H corresponds to a steeper stress decay and thus a more brittle post-peak response. Physically, this softening behavior is governed by the interplay between matrix embrittlement and confinement constraints. Extended curing densifies the gel network, leading to a rapid release of stored elastic energy upon failure (steeper softening), whereas higher confining pressure restricts lateral dilation and promotes frictional sliding, thereby sustaining the residual load-bearing capacity (gradual softening). It is important to note that the post-peak softening behavior is not solely an intrinsic material property but is also influenced by the stiffness of the testing system relative to the specimen. Consequently, the derived parameters H and B should be interpreted as comparative indices characterizing the relative ductility under the specific boundary conditions of this study, rather than as absolute material constants transferable to different loading environments. In this study, H is treated as an intermediate descriptor of the post-peak behavior and has been determined for all testing conditions, as summarized in Table 2.

Because the apparent magnitude of H is influenced by the pre-peak stiffness level, it is normalized using a reference stiffness derived from the fractional constitutive relation in the pre-damage domain. According to Eq. (15), the stress–strain relation before damage can be written as

$$\sigma(\varepsilon) = \mathbb{K}\,\varepsilon^{1-\alpha} \tag{16}$$

which yields the tangent stiffness

$$\frac{d\sigma}{d\varepsilon} = (1-\alpha)\,\mathbb{K}\,\varepsilon^{-\alpha} \tag{17}$$

Evaluated at the peak strain ε_c, the reference stiffness is therefore

$$E_c = (1-\alpha)\,\mathbb{K}\,\varepsilon_c^{-\alpha} \tag{18}$$

Using this quantity, a dimensionless post-peak softening (brittleness) index is defined as

$$B = \frac{H}{E_c} = \frac{H}{(1-\alpha)\,\mathbb{K}\,\varepsilon_c^{-\alpha}} = \frac{H\,\varepsilon_c^{\alpha}}{(1-\alpha)\,\mathbb{K}} \tag{19}$$

This index provides a consistent measure of post-peak softening severity that is independent of the absolute stiffness level of the material.

To link the post-peak response with the damage-induced microstructural evolution, the fractal-dimension increment is defined as

$$\Delta D_f = D_{f0} - D_f \tag{20}$$

where D_{f0} is the initial pore fractal dimension of the intact material and $D_f$is the fractal dimension measured after failure. Mathematically, ΔD_f quantifies the extent of topological degradation. Since the fractal dimension reflects the space-filling capacity of the pore network, a significant positive ΔD_f signifies a collapse in structural complexity, where the originally intricate three-dimensional void system degrades into simple, lower-dimensional planar fractures characteristic of brittle failure. Conversely, a value near zero or below indicates that high confinement promotes distributed micro-cracking. These micro-cracks generate new rough surfaces that compensate for the loss of original pores, thereby preserving the overall structural complexity associated with ductile deformation.

The relationship between the post-peak softening index B and the fractal-dimension increment ΔD_f is presented in Fig. 15. Despite the inherent scatter associated with post-failure measurements, a clear monotonic trend is observed: specimens exhibiting larger ΔD_f generally show more negative values of B, corresponding to a sharper post-peak softening response. Conversely, when ΔD_f approaches zero or becomes negative, B tends to be closer to zero, indicating a more stabilized post-peak behavior. The strength of this monotonic association is quantified using Spearman's rank correlation, yielding a high coefficient of $\rho = 0.876$ with a significance level of $p < 10^{-5}$. This strong correlation reveals the topological origin of ductility: a large positive ΔD_f signifies the collapse of the complex load-bearing network into simple planar fractures, which fail to sustain stress and cause a precipitous drop in load-bearing capacity (highly negative B). Conversely, a minimal ΔD_f implies that the damage distributes into a complex network of shear bands, thereby maintaining frictional contact and enabling a gradual, stable softening response.

5. Discussion

The experimental and theoretical investigations presented in this study demonstrate that the mechanical behavior of loess–slag backfill cannot be interpreted as a simple superposition of curing time and stress state. Instead, it emerges from a coupled multi-scale process governed by the evolution of fractal topology and deformation-induced energy dissipation. By integrating pore-scale fractal characterization, acoustic emission (AE) scaling analysis, and fractional-order constitutive modeling, this work establishes a mechanistic framework that clearly separates intrinsic strength generation from extrinsic failure control. This dual-control mechanism, and its cross-scale interactions, are schematically summarized in Fig. 16.

The intrinsic load-bearing capacity of the backfill originates from the curing-driven evolution of its static pore topology. As revealed by the MIP results, hydration progressively transforms the initially loose, macropore-dominated structure into a densified and interconnected gel network. This transformation is not merely a volumetric compaction process, but a topological reorganization that enhances the spatial

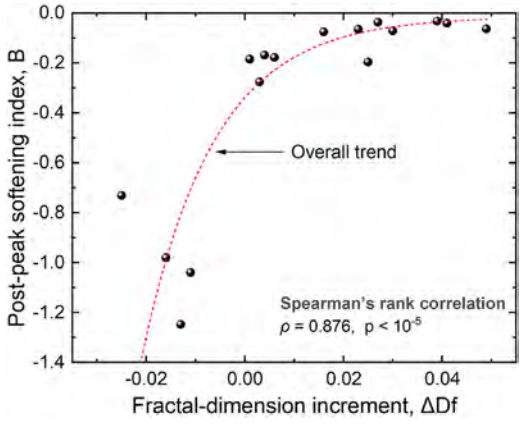

Fig. 15. Correlation between the post-peak softening index $\boldsymbol{B}$ and the damage-induced fractal-dimension increment $\boldsymbol{\Delta D_f}$.

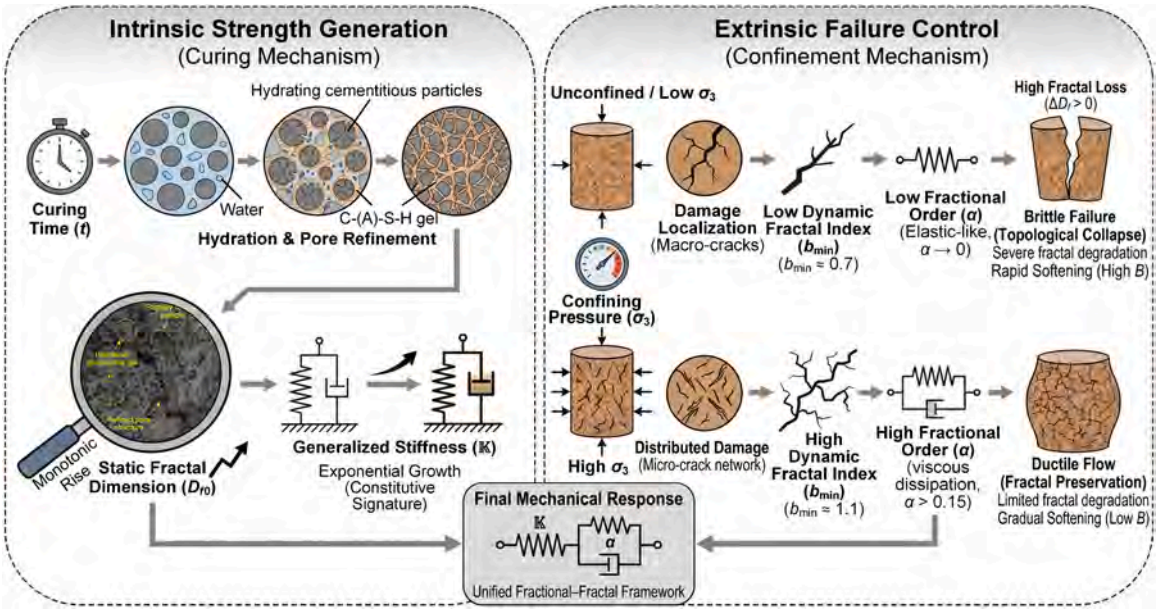

Fig. 16. Mechanistic model of the dual-control fractal-fractional response in loess-slag.

complexity of the solid skeleton. Such evolution is quantitatively captured by the monotonic increase in the initial fractal dimension (D_{f0}), which reflects the space-filling efficiency and connectivity of the load-bearing framework. The strong non-linear dependence between D_{f0} and the generalized stiffness $\mathbb{K}$ confirms that the pre-damage elastic response is fundamentally constrained by the fractal topology of the hardened matrix. As illustrated in the left panel of Fig. 16 ("Intrinsic Strength Generation"), curing time constructs a high-dimensional fractal skeleton that defines the potential stiffness and strength of the backfill through an exponential constitutive signature.

However, the realization of this intrinsic potential—particularly whether the material fails in a brittle or ductile manner—is governed by the dynamic fractal characteristics of damage evolution under confinement. AE analysis reveals that damage accumulation in loess–slag backfill follows scale-invariant statistics, yet the associated scaling laws are highly sensitive to the stress environment. Under unconfined or low-confinement conditions, the minimum b-value (b_{min}) remains low, indicating a dominance of large-scale, localized cracking events. This damage mode corresponds to a topological collapse of the initially three-dimensional microstructural network into a limited number of preferential fracture planes, as depicted in the brittle path of Fig. 16. Such dimensional reduction restricts the continuity of deformation pathways and suppresses stress redistribution, leading to a rapid loss of load-carrying capacity.

In contrast, high confining pressure fundamentally alters the damage evolution pathway. By suppressing tensile crack opening and promoting frictional sliding and shear interaction among micro-cracks, confinement enforces a distributed damage network with higher fractal complexity. This preservation of damage topology is reflected by elevated b_{min} values and maps directly to an increased fractional order α. From a physical perspective, α therefore represents a rheological index that characterizes the degree of deformation memory associated with distributed micro-crack interactions, rather than a purely mathematical fitting parameter. As shown in the ductile branch of Fig. 16, confinement prevents topological collapse and enables the material to sustain stable fractional-order deformation prior to peak failure.

The post-peak response further consolidates this interpretation. The strong Spearman rank correlation between the post-peak softening index B and the fractal-dimension increment (ΔD_f) demonstrates that macroscopic ductility is essentially governed by the degree of fractal preservation during failure. Brittle specimens exhibit a pronounced fractal collapse (large ΔD_f), which manifests as a steep post-peak stiffness degradation and rapid softening. Conversely, under sufficient confinement, ΔD_f approaches zero, indicating that the material retains its topological integrity even after peak stress. This preserved fractal framework allows the backfill to sustain residual load through a reorganized but still highly connected shear structure, resulting in gradual post-peak softening characterized by low index *B*.

Taken together, the mechanism illustrated in Fig. 16 provides a unified physical interpretation linking microstructural densification, dynamic damage scaling, and fractional constitutive response. The results highlight that curing controls the capacity of the material through static fractal topology, while confinement governs the realization of this capacity by regulating damage dimensionality and deformation memory. This dual-control fractal–fractional framework offers a physically grounded basis for tailoring the strength and ductility of cemented backfill materials through coordinated microstructural design and stress-path optimization.

6. Conclusions

This study systematically investigated the mechanical response of loess–slag backfill by integrating pore-scale fractal characterization, acoustic emission (AE) scaling analysis, and fractional-order constitutive modeling. By strictly separating the pre-damage hardening stage from post-peak failure, the intrinsic material evolution and extrinsic stress control mechanisms were decoupled and quantified. The main conclusions can be summarized as follows:

(1) Curing-driven pore-topology evolution governs intrinsic stiffness generation. Mercury intrusion porosimetry revealed that curing induces a continuous refinement of the pore network rather than a simple reduction in porosity. This topological evolution is effectively quantified by the initial pore fractal dimension D_{f0}, which increases monotonically with curing time. A strong non-linear relationship was established between D_{f0} and the generalized stiffness $\mathbb{K}$, demonstrating that the pre-damage elastic resistance of the backfill is fundamentally controlled by the space-filling complexity of the hydrated solid skeleton.

(2) Damage evolution exhibits scale-invariant characteristics strongly dependent on confinement. Acoustic emission analysis showed that microcrack accumulation follows fractal scaling

laws, with the minimum AE b-value ($b_{\min}$) serving as a sensitive indicator of damage localization. Low confinement promotes the dominance of large-scale cracking events, while high confinement sustains a distributed microcrack network. This transition reflects a change in the dynamic fractal organization of damage rather than a change in damage intensity alone.

(3) The fractional order α has a clear physical interpretation linked to damage topology. The fractional-order constitutive model, calibrated exclusively within the stable hardening regime, demonstrated excellent agreement with experimental stress–strain data. Beyond its mathematical role, the fractional order $\alpha$was shown to correlate strongly with $b_{\min}$, indicating that αrepresents the degree of deformation memory associated with distributed versus localized damage. Higher αvalues correspond to sustained microcrack interaction and enhanced ductility under confinement.

(4) Post-peak softening is governed by fractal preservation rather than peak strength. The post-peak softening index $B$was found to correlate strongly with the fractal-dimension increment ΔD_f, as confirmed by Spearman's rank analysis. Severe softening is associated with significant fractal loss, indicating topological collapse of the load-bearing network. In contrast, specimens exhibiting minimal ΔD_f retained higher residual capacity and gradual softening, highlighting that ductility is essentially the ability to preserve fractal complexity during failure.

(5) A unified fractional–fractal framework captures both pre- and post-peak behavior. By linking static pore fractal structure (D_{f0}), dynamic damage scaling ($b_{\min}$), fractional constitutive parameters ($\mathbb{K}$ and α), and post-peak softening behavior (B), a coherent multi-scale interpretation of backfill mechanics is achieved. This framework clarifies how intrinsic microstructural evolution and extrinsic confinement jointly determine stiffness development, deformation mode, and failure stability.

Overall, the results demonstrate that the mechanical performance of loess–slag backfill is governed by fractal topology and its evolution across scales. Rather than treating strength, ductility, and softening as independent properties, this study provides a physically grounded perspective in which these macroscopic behaviors emerge from the preservation or degradation of structural complexity. Practically, this advocates for a dual-control strategy in backfill design: curing management must be prioritized to ensure sufficient intrinsic stiffness for minimizing roof subsidence, whereas the confinement provided by the surrounding rock should be leveraged to enhance ductility and prevent burst-prone collapse. Finally, regarding engineering implementation, the identified AE fractal scaling laws offer a non-destructive quantitative criterion for early warning. Future engineering applications can leverage microseismic monitoring systems to track these b-value precursors in situ, providing real-time safety assessments for deep backfill stopes.

Data availability

The datasets used and/or analyzed in the current studies are available from the corresponding author on reasonable request.

CRediT authorship contribution statement

Haoyan Lyu: Writing – original draft, Visualization, Methodology, Investigation, Formal analysis, Data curation, Conceptualization. **Peng Wu:** Writing – review & editing, Methodology, Investigation, Funding acquisition, Data curation, Conceptualization. **Lianying Zhang:** Supervision, Resources, Funding acquisition. **Hideki Shimada:** Writing – review & editing, Resources. **Takashi Sasaoka:** Writing – review & editing, Supervision. **Akihiro Hamanaka:** Writing – review & editing.

Declaration of competing interest

The authors declare that they have no known competing financial interests or personal relationships that could have appeared to influence the work reported in this paper.

Acknowledgements

This work was supported by the National Natural Science Foundation of China (52274140, 52304102); Xuzhou Key Research and Development Plan (Social Development), Project Number: KC23314; Xuzhou University of Technology's school-local integration project (XKY2025114); China Scholarship Council (CSC).

Data availability

Data will be made available on request.

References

[1] X. Zhou, X.D. Zhao, Q.D. Qu, J.Y. Shi, Stope structural parameters design towards green and deep mining: a review, Processes 11 (11) (2023), https://doi.org/10.3390/pr11113125.
[2] C. Fairhurst, Some challenges of deep mining, Engineering 3 (4) (2017) 527, https://doi.org/10.1016/J.ENG.2017.04.017.
[3] G.L. Xue, E. Yilmaz, Y.D. Wang, Progress and prospects of mining with backfill in metal mines in China, Int. J. Miner. Metall. Mater. 30 (8) (2023) 1455, https://doi.org/10.1007/s12613-023-2663-0.
[4] C. Qi, A. Fourie, Cemented paste backfill for mineral tailings management: review and future perspectives, Miner. Eng. 144 (2019) 106025, https://doi.org/10.1016/j.mineng.2019.106025.
[5] L. Bo, S. Yang, Y. Liu, Z. Zhang, Y. Wang, Y. Wang, Coal mine solid waste backfill process in China: current status and challenges, Sustainability. 15 (18) (2023) 13489, https://doi.org/10.3390/su151813489.
[6] J. Wu, S. Yang, M. Williamson, H.S. Wong, T. Bhudia, H. Pu, Q. Yin, D. Ma, W. Chen, Microscopic mechanism of cellulose nanofibers modified cemented gangue backfill materials, Adv. Compos. Hybrid. Mater. 8 (2025). DOI.
[7] H. Liu, M. Fall, Consolidation and mechanical response of cemented tailings backfill to multiaxial stresses from rockwall closure and self-loading, J. Rock Mech. Geotech. Eng. (2025), https://doi.org/10.1016/j.jrmge.2025.07.013.
[8] W. Xu, Q. Li, B. Liu, Coupled effect of curing temperature and age on compressive behavior, microstructure and ultrasonic properties of cemented tailings backfill, Constr. Build. Mater. 237 (2020) 117738, https://doi.org/10.1016/j.conbuildmat.2019.117738.
[9] T. Liu, L. Chen, P. Wu, K. Zhang, L. Zhang, T. Jiang, L. Fu, Numerical simulation study on mesoscopic mechanism of fracture evolution of slag-loess-based cemented backfill material, Front. Mater. 12 (2025), https://doi.org/10.3389/fmats.2025.1646233.
[10] H.Y. Lv, Y.L. Chen, Q.H. Xie, P. Wu, Y.G. Chen, J. Gu, H.S. Wu, Performance optimization and characterization of loess-slag-based geopolymer composite: a new sustainable green material for backfill, Constr. Build. Mater. 354 (2022), https://doi.org/10.1016/j.conbuildmat.2022.129103.
[11] H. Lyu, Y. Chen, H. Pu, F. Jv, P. Wu, H. Shimada, T. Sasaoka, A. Hamanaka, Damage evolution laws and constitutive model description of loess-slag-based cemented backfill material, Constr. Build. Mater. 495 (2025) 143547, https://doi.org/10.1016/j.conbuildmat.2025.143547.
[12] N.M. Chiloane, F.K. Mulenga, Revisiting factors contributing to the strength of cemented backfill support system: a review, J. Rock Mech. Geotech. Eng. 15 (6) (2023) 1615, https://doi.org/10.1016/j.jrmge.2022.07.007.
[13] S.K. Behera, D.P. Mishra, P. Singh, K. Mishra, S.K. Mandal, C.N. Ghosh, R. Kumar, P.K. Mandal, Utilization of mill tailings, fly ash and slag as mine paste backfill material: review and future perspective, Constr. Build. Mater. 309 (2021), https://doi.org/10.1016/j.conbuildmat.2021.125120.
[14] L.H. Yang, J.C. Li, H.B. Liu, H.Z. Jiao, S.H. Yin, X.M. Chen, Y. Yu, Systematic review of mixing technology for recycling waste tailings as cemented paste backfill in mines in China, Int. J. Miner. Metall. Mater. 30 (8) (2023) 1430, https://doi.org/10.1007/s12613-023-2609-6.
[15] L. Yang, W. Xu, E. Yilmaz, Q. Wang, J. Qiu, A combined experimental and numerical study on the triaxial and dynamic compression behavior of cemented tailings backfill, Eng. Struct. 219 (2020) 110957, https://doi.org/10.1016/j.engstruct.2020.110957.
[16] W. Xu, B. Liu, W. Wu, Strength and deformation behaviors of cemented tailings backfill under triaxial compression, J. Cent. South. Univ. 27 (12) (2020) 3531, https://doi.org/10.1007/s11771-020-4568-7.
[17] J. Kim, S. Choi, A fractal-based approach for reconstructing pore structures of GGBFS-blended cement pastes, Constr. Build. Mater. 265 (2020) 120350, https://doi.org/10.1016/j.conbuildmat.2020.120350.
[18] Y. Gao, K. Wu, Q. Yuan, Limited fractal behavior in cement paste upon mercury intrusion porosimetry test: analysis and models, Constr. Build. Mater. 276 (2021) 122231, https://doi.org/10.1016/j.conbuildmat.2020.122231.

[19] X. Zhang, Y. Wei, J. Zuo, Y. Luo, B. Wang, W. Yao, Segmented fractal pore structure in cement-based materials blended with dolomite powder, J. Mater. Civ. Eng. 33 (11) (2021), https://doi.org/10.1061/(asce)mt.1943-5533.0003944.
[20] X. Han, J. Feng, and B. Wang, Relationship between fractal feature and compressive strength of fly ash-cement composite cementitious materials, cement and Concrete composites, 139(2023), p. 105052. DOI: 10.1016/j.cemconcomp.2023.105052.
[21] F. Yan, K. Luo, J. Ye, W. Zhang, J. Chen, X. Ren, Z. Liu, J. Li, Effect of pore structure characteristics on the properties of red mud-based alkali-activated cementitious materials, J. Sustain. Cen.-Based Mater. 13 (12) (2024) 1753, https://doi.org/10.1080/21650373.2024.2407990.
[22] L. Zeng, J. Zhu, Y. Zhao, S. Wang, H. Huang, J. Zhang, J. Ye, Pore structure characteristics and permeability analysis of natural anhydrite with various water /anhydrite ratios based on mercury intrusion porosimetry, Constr. Build. Mater. 398 (2023) 132422, https://doi.org/10.1016/j.conbuildmat.2023.132422.
[23] Y. Zhang, K. Wu, Z. Yang, G. Ye, A reappraisal of the ink-bottle effect and pore structure of cementitious materials using intrusion-extrusion cyclic mercury porosimetry, Cem. Concr. Res. 161 (2022) 106942, https://doi.org/10.1016/j.cemconres.2022.106942.
[24] Y. Chen, L. Dong, G.M. Adinolfi, J. Guo, Y. Zhang, S. Vinciguerra, Acoustic emission and wave velocity monitoring of rock-backfill composites: damage identification and failure characterization, Measurement 256 (2025) 118247, https://doi.org/10.1016/j.measurement.2025.118247.
[25] J. Wang, J. Fu, W. Song, Y. Zhang, S. Wu, Acoustic emission characteristics and damage evolution process of layered cemented tailings backfill under uniaxial compression, Constr. Build. Mater. 295 (2021) 123663, https://doi.org/10.1016/j.conbuildmat.2021.123663.
[26] L. Wang, J. Xie, D. Qiao, J. Wang, F. Huang, Damage evolution model of cemented tailing backfill based on acoustic emission energy, IOP Conf. Series 631 (1) (2021) 12071, https://doi.org/10.1088/1755-1315/631/1/012071.
[27] H. Huang, Y. Zhou, Y. Zhang, C. Wang, J. Bi, Anisotropic crack evolution and fractal failure mechanism of Lushan shale under compression: insights from acoustic emission, Sci. Rep. 15 (1) (2025), https://doi.org/10.1038/s41598-025-98695-5.
[28] L. Yuan-Hui, L. Jian-Po, Z. Xing-Dong, Y. Yu-Jiang, Study On B-Value and Fractal Dimension of Acoustic Emission During Rock Failure Process, Yantu lixue, 2009.
[29] H.R. Nejati, A. Nazerigivi, M. Imani, A. Karrech, Monitoring of fracture propagation in brittle materials using acoustic emission techniques-A review, Comput. Concr. 25 (1) (2020) 15, https://doi.org/10.12989/CAC.2020.25.1.015.
[30] Z. Ren, X. Qin, Q. Zhang, Y. Sun, Nonlinear mixed hardening constitutive model considering coupling damage under multiaxial non-proportional loading conditions, Iranian J. Sci. Technol., Transac. Mechan. Eng. 49 (1) (2024) 299, https://doi.org/10.1007/s40997-024-00793-8.
[31] Z. Luo, D. Airey, Y. Fu, A constitutive model for cemented granular materials capturing bond degradation, Comput. Geotech. 176 (2024) 106716, https://doi.org/10.1016/j.compgeo.2024.106716.
[32] Y. Feng, D. Fu, Y. Wang, Fractional Hardening-Damage Constitutive Model of Creep Characteristics On Cemented Backfill Material Under Step Loading, Front. Physics, 2025.
[33] Y. Feng, Y. Wang, J. Wu, Stress-dependent variable-order fractional constitutive model of cemented backfill materials and its parameter inversion with PSO: unified representation of creep processes, Commun. Nonlinear. Sci. Numer. Simul. 153 (2026) 109502, https://doi.org/10.1016/j.cnsns.2025.109502.
[34] Y. Wang, Y. Feng, H. Pu, Q. Yin, D. Ma, J. Wu, Step-variable-order fractional viscoelastic-viscoinertial constitutive model and experimental verification of cemented backfill, Acta Mech. 234 (3) (2022) 871, https://doi.org/10.1007/s00707-022-03416-y.
[35] Y. Gao, D. Yin, B. Zhao, A variable-order fractional constitutive model to characterize the rate-dependent mechanical behavior of soft materials, Fractal Fract 6 (10) (2022) 590, https://doi.org/10.3390/fractalfract6100590.
[36] K. Ding, C. Zeng, Study on the compressive strength, pore structure characteristics, and fractal dimension of the ecological porous concrete specimens based on ordinary Portland cement, Constr. Build. Mater. 483 (2025) 141795, https://doi.org/10.1016/j.conbuildmat.2025.141795.
[37] W. Peixin, C. Ping, W. Min, C. Yu, W. Congcong, Post-peak Stress-Strain Relationship Model of Rock Considering Confining Pressure Effect, Journal of Central South University (Science and Technology, 2017. DOI.
[38] Y. Zong, L. Han, D. Zhu, Y. Jin, M. Tian, Experimental investigation on post-peak strength and deformation behavior of cracked sandstone, Arabian J. Geosci. 13 (10) (2020), https://doi.org/10.1007/s12517-020-05379-7.
[39] G. Xu, H. Liu, B. Fu, J. Yu, Research and prospect of post-peak strain-softening characteristics of rocks, IOP Conf. Ser. 787 (1) (2021) 12135, https://doi.org/10.1088/1755-1315/787/1/012135.
[40] M. Bao, Z. Zhou, Z. Chen, L. Zhang, Creep constitutive model for damaged soft rock based on fractional-order nonlinear theory, J. Mt. Sci. 22 (6) (2025) 2276, https://doi.org/10.1007/s11629-024-9292-6.
[41] M. Jafari, X. Song, M. Grabinsky, Development of a method to predict the nonlinear mechanical response of cemented paste backfill to mining induced closure strains, Rock. Mech. Rock. Eng. 58 (8) (2025) 9435, https://doi.org/10.1007/s00603-025-04595-5.
[42] H. Liu, M. Fall, Mechanical response and pore pressure evolution of cemented paste backfill under deep mine-like multiaxial stress and temperature conditions, Int. J. Min. Sci. Technol. (2025), https://doi.org/10.1016/j.ijmst.2025.09.013.
[43] J. Matsimbe, M. Dinka, D. Olukanni, I. Musonda, Geopolymer: a systematic review of methodologies, Materials. (Basel) 15 (19) (2022), https://doi.org/10.3390/ma15196852.
[44] H. Lyu, Y. Chen, H. Pu, F. Ju, K. Zhang, Q. Li, P. Wu, Dynamic properties and fragmentation mechanism of cemented tailings backfill with various particle size distributions of aggregates, Constr. Build. Mater. 366 (2023) 130084, https://doi.org/10.1016/j.conbuildmat.2022.130084.
[45] J. Wu, M. Feng, X. Mao, J. Xu, W. Zhang, X. Ni, G. Han, Particle size distribution of aggregate effects on mechanical and structural properties of cemented rockfill: experiments and modeling, Constr. Build. Mater. 193 (2018) 295, https://doi.org/10.1016/j.conbuildmat.2018.10.208.
[46] Y. Wang, M. Wang, C. Tang, Y. Yu, S. Chen, Study on the triaxial compressive properties of alkali activated concrete after freeze-thaw cycles, Sci. Rep. 15 (1) (2025) 20517, https://doi.org/10.1038/s41598-025-06337-7.
[47] E. Hoek, E.T. Brown, Empirical strength criterion for rock masses, J. Geotechn. Eng. Divis. 106 (9) (1980) 1013, https://doi.org/10.1061/AJGEB6.0001029.
[48] P.K. Mehta and P.J. Monteiro, *Concrete microstructure, properties, and Materials*, McGraw-hill, 2006.
[49] T. Luping, L. Nilsson, A study of the quantitative relationship between permeability and pore size distribution of hardened cement pastes, Cem. Concr. Res. 22 (4) (1992) 541, https://doi.org/10.1016/0008-8846(92)90004-F.
[50] L. Jiang, Y. Guan, Pore structure and its effect on strength of high-volume fly ash paste, Cem. Concr. Res. 29 (4) (1999) 631, https://doi.org/10.1016/S0008-8846(99)00034-4.